



Influence of the temperature–time regime on the mechanical properties during the DED-Arc process of near-net-shape Ti-6Al-4 V components

Maximilian Gierth¹ · Nils Michael¹ · Philipp Henckell¹ · Jan Reimann¹ · Jörg Hildebrand¹ · Jean Pierre Bergmann¹

Received: 5 September 2022 / Accepted: 5 March 2023 / Published online: 11 May 2023
© The Author(s) 2023

Abstract

In a research project, the additive manufacturing process of components made of Ti-6Al-4 V using gas metal arc welding (GMAW), which is classified into the directed energy deposition–arc (DED-Arc) processes, was investigated. The project focused on the systematic development of economical additive build-up strategies and the analysis of the temperature–time regime during the build-up process, as well as the investigation of the resulting properties. A welding range diagram was created with recommendations for process settings for additive manufacturing with the controlled short circuit, as well as a presentation of possible defect patterns outside the range shown. For the fabrication of thick-walled structures, various build-up strategies were investigated by modifying the welding path and evaluated with regard to their suitability. Based on the results, additive structures were fabricated by varying the temperature–time regime in order to gain insights into selected geometrical, metallurgical, and mechanical properties. Different energy inputs per unit length, structure dimensions, and interpass temperatures (IPT) were used for this purpose. The research project provides comprehensive findings on the additive processing of the material Ti-6Al-4 V using metal inert gas welding, in particular with regard to the temperature–time regime and the resulting properties.

Keywords DED-Arc · GMAW · Ti-6Al-4 V · Temperature–time regime · Mechanical properties

1 Introduction

Titanium and its alloys are of particular industrial interest due to their specific properties, such as low density combined with high strength, very good corrosion resistance, and biocompatibility. In general, they are used primarily in aerospace, energy technology, automotive engineering, and medical technology applications. The alloy Ti-6Al-4 V is the most widely used titanium alloy, accounting for about 50% of global production [1].

A limiting factor in the industrial use of titanium and its alloys is the high cost. Accordingly, the aim is to use as little material as possible on the way from the raw material used to the final component. This is achieved by keeping

the “buy-to-fly” ratio as low as possible. In this context, the use of additive manufacturing makes it possible to increase material utilization from approx. 8% in conventional manufacturing processes (e.g., turning, milling) to up to 33% [2].

The directed energy deposition–arc (DED-Arc) process in conjunction with gas metal arc welding (GMAW) represents a cost-effective type of additive processing due to the comparatively simple equipment and the use of wire material compared to powder-based processes, while at the same time, high build rates can be achieved. Furthermore, significantly higher energy efficiency is achieved than with laser- or electron beam-based processes [3].

The advantages of DED-Arc are offset by a large number of challenges with regard to process control, post-processing, and adjustment of the resulting microstructure, particularly in the processing of titanium and titanium alloys. Compared to beam-based processes, the process-specific energy input and thus the heat input for DED-Arc can be considered high [4]. At the same time, Ti-6Al-4 V has a low thermal conductivity of approx. 6.8 W/mK at room temperature up to approx. 25 W/mK at 1540 °C [5]. The combination of these

Recommended for publication by Commission I—Additive Manufacturing, Surfacing, and Thermal Cutting

✉ Maximilian Gierth
maximilian.gierth@tu-ilmenau.de

¹ Technische Universität Ilmenau, Ilmenau, Germany

characteristic properties results in a constant heat increase in the built-up structure due to the recurring heat input during the layer build-up and has an influence on the temperature regime or the cooling behavior of the individual layers [6]. This is currently a limiting factor in effective processing using the GMAW process [7].

Simultaneously, the formation of anisotropic mechanical properties, in particular strength and elongation properties, as well as fracture and fatigue crack behavior, is favored [7–12]. This results from the growth of the previous β -grains along the build-up direction and temperature gradient and from the formation of different microstructures of the α -titanium due to different heating and cooling rates [13, 14].

A large number of previous studies have dealt with the influence of process input variables, such as energy input or wire feed, and path planning on the resulting geometrical, metallurgical, or mechanical component properties. However, most of these publications use TIG [15–18] or plasma processes [19–21]. Baufeld et al. and Brandl et al. further compare a wire-based additive laser process with an additive TIG process [22, 23]. They conclude that both processes are suitable for additive manufacturing and that the mechanical properties of cast material and, after suitable post-heat treatment, even those of forged material are achieved and surpassed. The TIG process stands out due to partially higher elongations at break [22]. This comparison was also carried out by Almeida et al. and Tabernero et al. within the arc-based additive processes [24, 25]. Here, in addition to the TIG and plasma processes, the conventional GMAW process and the energy-reduced, controlled GMAW process with reversing wire movement (cold metal transfer—abbreviated CMT) were used. Almeida et al. came to the conclusion that the CMT process is also suitable for large-volume components and that finer β -grains are formed due to the lower heat input compared to the TIG process [24]. Furthermore, Tabernero et al. were able to show that although high build-up rates can be achieved with the CMT process, but the anisotropy of the mechanical properties is most pronounced. Additionally, helium-containing shielding gas compositions should be used to generate suitable aspect ratios for overlaps [25]. Other studies are addressing the instability and wandering of the arc and spatter-generating material transition present in the GMAW process when processing Ti-6Al-4 V. This is due in part to the wandering of the cathode spots as a result of the material properties [26]. In the CMT process, the phenomenon of arc blow is also evident, which is caused, for example, by the migration of the cathode spot between the substrate plate and the weld metal [27]. An increase in process stability using CMT can be achieved by an additional laser directed at the process [28], by using an oxidized welding wire [29] or by negative polarity of the wire electrode [30]. In a comparison of the CMT process (controlled short circuiting with

reversing wire motion) with a controlled short circuiting and a self-regulating arc with negatively poled wire electrode, Panchenko et al. concluded that the best results in terms of material utilization or final contour proximity of thin-walled additive structures can be achieved with the controlled short circuiting without reversing wire motion. This is due to the short arc length and sufficient heat supply during the burning phase [31]. Nevertheless, the use of the controlled short circuiting with reversing wire motion and specifically the CMT process is widely used for additive processing of Ti-6Al-4 V due to its positive properties. Its suitability is documented in various publications [24, 25, 32–34].

However, only a small number of studies exist so far, which deal with the influence of the temperature–time regime (e.g., interpass temperature or cooling rate) during additive manufacturing by CMT on the resulting component properties [13, 34, 35]. Li varied the interpass temperature up to 300 °C. He concluded that an increase in interpass temperature is comparable to an increase in heat input with respect to weld penetration and weld bead geometry. With the increase of interpass temperature, the oxidation of the surface increases. At the same time, the proportion of β -phase decreases. This results in no significant differences in hardness and tensile strength, but the elongation at break is strongly reduced [34]. This is attributed by Li to oxygen uptake during the cooling process. In this respect, Vazquez et al. and Yi et al. found that a slow cooling rate, either caused by short dwell times or high interpass temperatures, strongly coarsens the grain boundary- α and the prior β -grains become strongly columnar. The result is a significant reduction in elongation at break. Accordingly, high cooling rates and low interpass temperatures are beneficial for the resulting mechanical properties [13, 35].

A variety of strategies were pursued to reduce the size of the former β -grains and achieve equiaxed grain structures. One option for grain refinement is the addition of additional elements, such as boron, silica, and carbon [36–40]. Birmingham et al. and Mereddy et al. were able to show that in the cooling process, the added, initially dissolved alloying elements segregate at the grain boundaries of the β -grains. The result is a constitutional supercooling of the melt, which results in a lateral growth restriction of the β -grains by the segregated elements. At the same time, more potential nucleation particles are present. Thus, a reduction in the size of the prior β -grains and a reduction in the α -lath length are possible [36–38]. In this regard, Birmingham et al. demonstrated quantitatively that the growth-restricting solutes reduce the grain size by more than 55%. Nevertheless, this does not lead to the formation of a significant fraction of equiaxed β -grain structures. By adding additional nucleating particles, such as La_2O_3 , the grain size can be reduced by 85% and zones of equiaxed grains can be formed, mainly at the top of the layer, with columnar grains at the base [39].

The actions result in an increase in elongation at break. After additional post-heat treatment, an increase in tensile strength in combination with a higher elongation at break is also possible.

Another approach for grain refinement is to introduce mechanical deformation in the additive build-up process, mostly between layer generations. This is done either by an interpass rolling process, by mechanical surface hammering, or by ultrasonic impact treatment. Due to the introduced deformation and the temperature-induced recrystallization during the next layer generation, short columnar and equiaxed β -grains are formed and improved and isotropic mechanical properties result [41–44]. The grain refining effect can be enhanced by enlarging and adjusting the roll geometry and the higher loads that can be realized [45]. A positive side effect of interpass rolling is the reduction of residual stresses and thus lower resulting component distortion [46]. In addition, an almost constant layer height can be achieved in the build-up process due to the deformation [47]. The advantage of mechanical surface hammering over rolling is greater potential geometric design freedom [48].

The third option for grain refinement and production of isotropic metallurgical and mechanical properties is the use of post-process heat treatments. For homogeneous microstructures with isotropic properties, very slow cooling rates (10^{-20} K/s) are necessary during the β α transformation. However, it is important to ensure that the temperatures or the process times are not too high or too long; otherwise, an equiaxed but also a coarse grain structure will result. This is related to a reduction in strength with simultaneously almost constant elongation at break [32, 33, 49].

Another challenge is the affinity of titanium to absorb atmospheric gases, especially oxygen, at temperatures above 500 °C and the associated growth of an oxide layer and the so-called “alpha case” which results in hardening or embrittlement of the material [6, 50–53]. Accordingly, it is important to shield the weld metal as completely as possible from atmospheric gases during solidification and cooling. This is done either by means of conventional trailing gas nozzles, shielding gas-flooded welding chambers, or novel developments, such as the local shielding device of Ding et al. [54]. Bermingham et al. investigated the influence of varying trailing gas compositions in the inert gas nozzle on the oxidation of the cooling molten bath by increasing the active gas content in the trailing gas (starting with 100% argon). In the last case, no trailing gas coverage was provided. It was found that there was no statistically relevant effect on the chemical compound of the alloy, tensile strength, or elongation at break, despite the formation of different surface states of the weld material (from metallic shiny to flaky brown oxide). The measured microhardness shows that the oxidized external surface extends a maximum of 100 μm into the component in the worst case with no

trailing gas coverage. This layer thickness is usually removed in the final machining of the components. It should be noted here that only small 4-layer structures were built and examined [55]. In order to avoid heat accumulation and to conduct the injected thermal energy out of the component as quickly as possible, a plate through which liquid flows was placed under the substrate in a cooling approach. A positive influence on manufacturing time and mechanical properties was observed [35].

In summary, much research work has already been conducted in the field of additive processing of Ti-6Al-4 V. However, there are only few systematic investigations on the economic use of different additive build-up strategies and hardly any findings on the process limits when using the DED-Arc by means of GMAW. Furthermore, there is limited information on the property characteristics of the generated structures depending on the heat input and the temperature–time regime or the cooling behavior for GMAW-based additive manufacturing of Ti-6Al-4 V. Systematic investigations on the influence of the interpass temperature on the CMT process and the resulting component properties were only performed by Lu, Yi et al., Vazquez et al., and Vazquez et al., which varied the dwell time between layer deposition between 0 and 9 min [34, 35]. Further investigations on temperature-controlled process control have the potential to enable a specific adjustment of the properties of the produced near-net-shape components by homogenizing the thermal field and to generate isotropic component properties. Consequently, the economic and sustainable attractiveness of the process can be significantly increased.

2 Aim of the investigation

The aim of the investigations was the systematic development of strategies for the specific adjustment of component properties during the additive manufacturing of Ti-6Al-4 V structures by means of the GMAW welding process. A homogeneous microstructure was to be set through controlled tempering of the structure to be manufactured. To achieve the goal, different build-up strategies were initially addressed as a starting point and process limits were evaluated. In the following, it was intended to generate additive wall structures with varied wall thicknesses using multi-row, meandering, or oscillating welding paths. At the same time, the main influencing variables of the welding process, such as wire feed or welding speed, could be adjusted. Additive wall structures were built up by varying the interpass temperature between 150 °C as the lower and 1050 °C as the upper limit temperature. The temperature–time regimes occurring during the additive build-up process were analyzed and

correlated with the resulting geometric, metallurgical, and mechanical properties. As a result of the investigations, new insights into the influence of varying interpass temperatures on the mechanical properties should be obtained, and a near-net-shape additive manufacturing of components made of Ti-6Al-4 V with homogeneous mechanical properties should be possible.

3 Experimental setup and methods

3.1 Materials and equipment

In order to carry out the welding trials, a Fronius CMT Advanced 4000 welding power source with a push–pull torch system and a 400-mm-long torch neck were used. Here, the energy-reduced, controlled short circuit process “cold metal transfer” (CMT) with reference number 1009 was selected as the welding characteristic, which is specifically designed for welding Ti-6Al-4 V. A Kuka KR 150–2000 6-axis industrial robot served as the handling system. The basic experimental setup can be seen in Fig. 1a (extended torch neck not shown). Due to the affinity of the titanium material for absorbing atmospheric gases, the welding tests were carried out in a shielding gas chamber, as shown in Fig. 1b. The absorption of oxygen, nitrogen, or hydrogen leads to a change in the microstructure or the mechanical properties. Gas absorption increases at temperatures $> 550\text{ }^{\circ}\text{C}$ [50]. The result is a hardening of the material with a simultaneous decrease in ductility. In particular, the hardening of the surface areas makes subsequent machining of the welded

components more difficult and should therefore be avoided by using a working atmosphere filled with inert gas.

The handling system is coupled via a flexible hood made of a temperature resistant and coated fabric. Viewing windows made of borosilicate glass are inserted on three sides of the chamber. These serve as an interface for process observation or monitoring by means of a high speed camera and pyrometer. The selected glass material is particularly suitable for this purpose due to its high thermal load capacity and high transmission of over 90% in the wavelength range between 0.3 and 2.3 μm . This represents the spectral range in which the relevant devices for optical temperature measurement operate.

The inert gas is introduced via four connecting holes that lead into a circumferential cavity. By means of a diffuser layer made of metal mesh or foam, a pressure gradient is created between the mentioned cavity and the welding chamber. This creates a laminar gas flow and ensures efficient displacement of the remaining air. As an indicator for the residual amount of atmospheric air components, the residual oxygen content in the chamber is measured with a JAeroF type oxygen monitor. For this purpose, there are measuring fittings near the substrate and in the upper area of the chamber, through which a flexible measuring tube can be led to desired measuring points inside. The inert gas atmosphere is created by the continuous introduction of argon 5.0 (according to Table 2). Due to the higher density of argon ($\rho \approx 1.784\text{ g/dm}^3$) compared to air ($\rho \approx 1.293\text{ g/dm}^3$), the inert gas displaces the atmospheric components through a relief valve at the top of the chamber. Conclusively, by measuring the residual oxygen content at the upper measuring port, the same or lower oxygen content can be guaranteed in areas of the chamber below. The

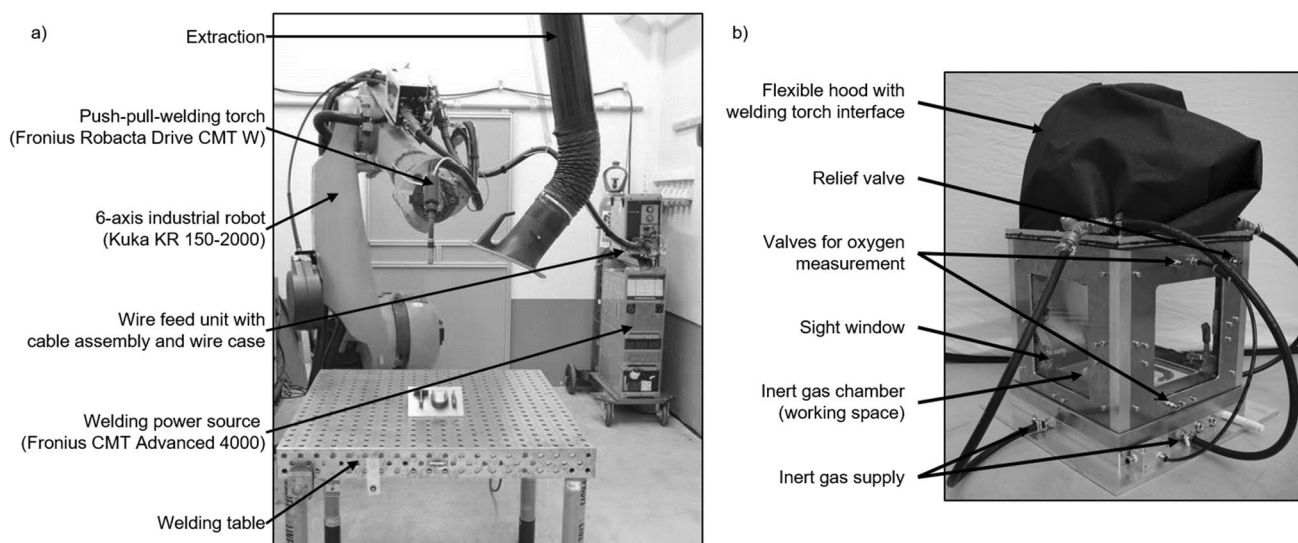


Fig. 1 a Test laboratory with equipment and b shielding gas chamber used for the investigations stating essential components

welding process is started after a residual oxygen content of 100 ppm has been reached. Preliminary investigations have shown that below this value, the formation of annealing colors on the surface of the titanium structures is avoided.

For the acquisition of the relevant welding data, such as welding current I or voltage U , a data acquisition system (DAQ system) called DEWE PCI-16 from Dewetron was used. In combination with the welding speed v_s , the energy input per unit length E_s is calculated according to Eq. (1). This can be used to evaluate the energy input during additive manufacturing with arc process.

$$E_s = \frac{P}{v_s} \left[\frac{\text{kJ}}{\text{cm}} \right] \text{mit } P = \int_0^t \frac{U * I}{dt} [\text{W}] \quad (1)$$

The temperature–time regime was measured with noncontact pyrometers. Therefore, a Metis M318 single-wavelength pyrometer from Sensortherm GmbH with a measuring range between 100 and 700 °C (measurement uncertainty: $\pm 0.5\% + 1$ K) and a M322 ratio pyrometer from the same company with a higher measuring range of 350–1300 °C (measurement uncertainty: $\pm 0.3\% + 2$ K) was used. Type C (tungsten-rhenium) tactile thermocouples were used to validate the optical temperature measurement. These have a wide measuring range between 0 and 2300 °C and a high melting point.

For the investigations, a titanium alloy Ti-6Al-4 V (titanium grade 5) with the material number 3.7165 is used as solid wire electrode with a diameter of $\varnothing_w = 1.0$ mm and with the specification according to AWS A5.16, ER Ti 5 or EN ISO 24034, S Ti 6402c and as substrate material with the specification according to ASTM B 265–00. Table 1 shows the chemical composition of the filler metal and substrate material used. Table 2 shows the names, the respective use, and the composition of the inert gases used.

3.2 Methodical and systematic approach

For the investigations of suitable build-up strategies for the additive build-up process using DED-Arc, small volume additive structures were built in the first step. According to Fig. 2, the structures were divided into thin- and thick-walled structures. If the required structure width is smaller than the

Table 2 Inert gases used with indication of use and their composition in volume percent according to DIN EN ISO 14175:2008

Category	Usage	Type—name	Composition
Inert gas	Shielding gas in chamber	I1—Ar 5.0	99.999 Ar
	Welding shielding gas	I3—ArHe30	30% He, bal. Ar
	Welding shielding gas	I3—ArHe70	70% He, bal. Ar

possible weld bead width of a stringer bead, the classification criteria for thin-walled structures is met. In this case, the structure width can be realized by single-row weld paths. Here, the potentially necessary machining post-processing for the generation of a planar side surface of the component is taken into account, as this is often necessary for the application. Multiple-row welding paths, such as multi-row, meandering, or oscillating, are used to build thick-walled structures. In this case, overlapping weld paths are used to create structures whose width is greater than a single line bead and can be adjusted as desired.

The additive build-up was carried out bidirectional, i.e., the start and end points of the welding process were alternated layer by layer. For the generation of the thin-walled structures, the additive build-up of three welding layers with a length of approx. 100 mm was carried out by varying the energy input per unit length. In a further step, the helium content in the welding gas was increased from 30 (ArHe30) to 70% (ArHe70) and the same series of experiments were conducted. The individual substrate plates had dimensions of 150 mm \times 25 mm \times 6 mm. Before applying a new layer, an interpass temperature of 100 °C was set and measured by means of a M318 pyrometer below the welding torch after layer generation. According to the occurrence of irregularities, weld range diagrams were generated as a function of the energy input per unit length. To validate the findings, a 30-layer wall structure per shielding gas with a length of approx. 120 mm was to be generated by using exemplary input variables, like welding speed and wire feed speed, within the recommended value range (see Fig. 11).

For the thick-walled structures, the multi-row weld sequences shown in Fig. 3a were considered. In this case, overlapping weld paths are used to produce structures whose width is greater than that of a single weld bead. Depending

Table 1 Chemical composition of the used molten filler wire material and of the substrate material according to mill certifications in mass fractions

	C	O	N	H	Fe	Al	V	Ti
Wire	0.05	0.13	0.03	0.015	0.22	6.3	3.5	bal
Substrate	0.16	0.17	0.02	0.0046	0.16	6.18	4.1	bal

Fig. 2 Systematic approach for building thin-walled and thick-walled additive structures

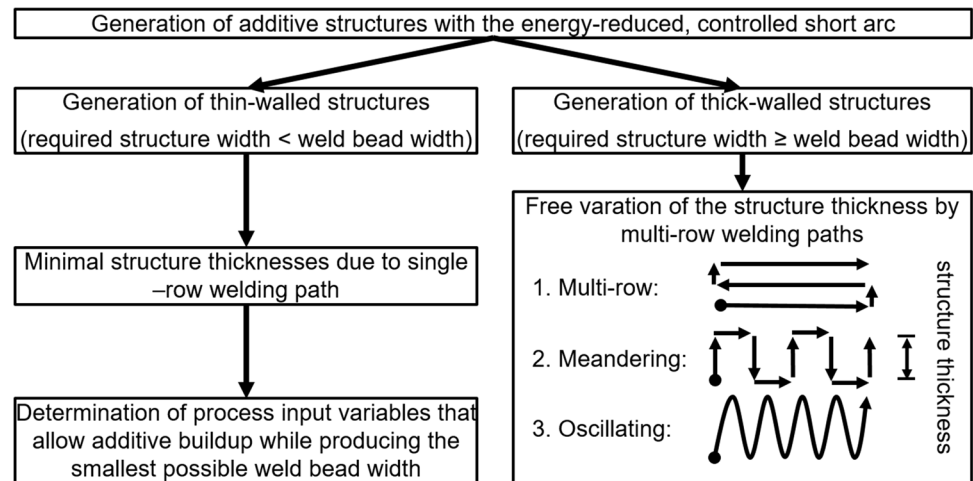
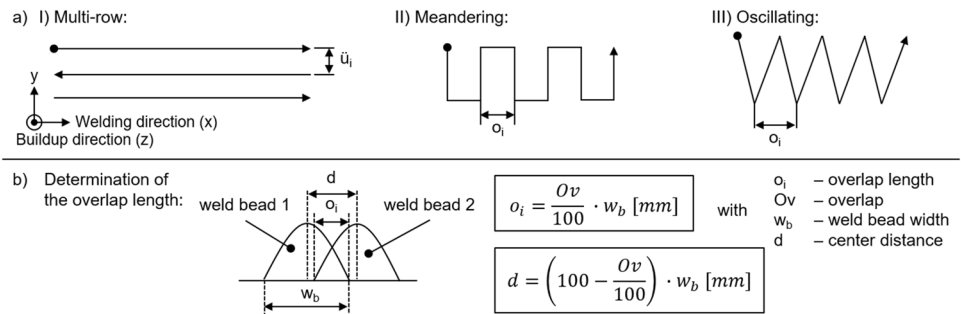


Fig. 3 Schematic illustration of **a** the welding paths for the different build-up strategies and definition of the overlap length o_i and **b** of the variables for determining the overlap length o_i



on the strategy used, the overlap length o_i , respectively center distance d , was defined as shown in Fig. 3a. Accordingly, the calculation of the overlap length o_i or center distance d is possible according to the equations in Fig. 3b for a given overlap Ov and determined weld bead width w_b [56, 57]. Using the various build-up strategies, additive wall structures with lengths between 70 and 120 mm and heights corresponding to 7 to 10 layers were built up with layer-by-layer alternating (bidirectional) change of the welding direction. Widths between 12 and 22 mm could be addressed. The welding pause between the applications of the individual layers was set to 3 min. ArHe30 and ArHe70 were used as shielding gases.

The degree of overlap was varied according to the build-up strategy as shown below:

- Multi-row build-up strategy: $Ov = 10\text{--}30\%$
- Meandering build-up strategy: $Ov = 10\text{--}50\%$
- Oscillating build-up strategy: $Ov = 0\text{--}30\%$

In order to evaluate the near-net-shape and to select a suitable build-up strategy as well as an overlap for the further experimental studies, selected structures were analyzed by means of 3D scans, inspected by visual inspection and metallographically examined for lack of fusions.

Based on the findings regarding the build-up strategies, a systematic investigation of varying temperature–time regimes and their influence on the resulting geometric,

metallurgical, and mechanical component properties was carried out using thick-walled structures as an example. A temperature-controlled process using defined interpass temperatures (IPT) was used for this purpose. This means that the additive build-up process is not continued until the temperature falls below the interpass temperature after a layer generation has been completed. The highest temperature of the last applied layer (top layer) serves as an adjustment criteria. Interpass temperatures between 150 and 1050 °C were addressed.

The structures were programmed with the nominal widths $w = 18$ mm and $w = 22$ mm by adjusting the pendulum width. At the same time, this changes, among other aspects, the energy input per layer and thus the heat input. Due to the extension of the necessary cooling times into the lower temperature ranges, it was decided not to produce the structures with an interpass temperature lower than 600 °C with the structure width of $w = 22$ mm, as it was not considered economical. Nevertheless, the tests showed that there is no significant difference in the resulting properties between the two widths of the thick-walled structures and thus no further findings can be generated. All wall structures have a length of about 180 mm and were generated using an alternating build-up strategy. The substrates with the dimensions 225 mm × 90 mm × 10 mm were fixed in the test room with hold-downs at the corner points. The specified welding

$E_S = 4.10$ kJ/cm; $v_W = 12.0$ m/min; $v_S = 0.4$ m/min; $U = 16$ V; CTWD = 14 mm; gas flow rate = 20 l/min, ArHe70	Thick walled structures (oscillating strategy)	
	18 mm structure width	22 mm structure width
Interpass temperature (IPT) [°C]	150, 300, 450, 600, 800	600, 800, 1050, 1300
Number of layers [-]	10	10
Structure length [mm]	180	180
Welding time per layer [s]	135	185
Welding distance per layer [mm]	900	1233
Total welding distance [mm]	9000	12333
Energy input per layer [kJ]	369	505,7
Melted wire per layer [m]	27	37
Melted wire mass per layer [g]	93	128,8

Fig. 4 Overview of the resulting characteristics of the generated thick-walled structures under variation of the structure width and the interpass temperature (IPT) with constant welding inputs

input variables resulted in an energy input per unit length of $E_S = 4.1$ kJ/cm and were not varied regardless of the structure width, resulting in mean stringer bead width of $w_b = 8$ mm. Figure 4 gives an overview of the generated structures and a selection of resulting characteristic values.

Fig. 5 a Comparison of the measured temperature curves for different types of measuring equipment when measuring through the borosilicate glass plane of the used shielding gas chamber and **b** the corresponding experimental setup

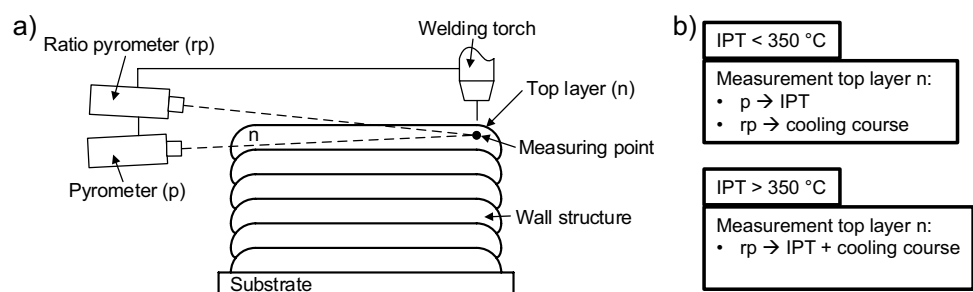
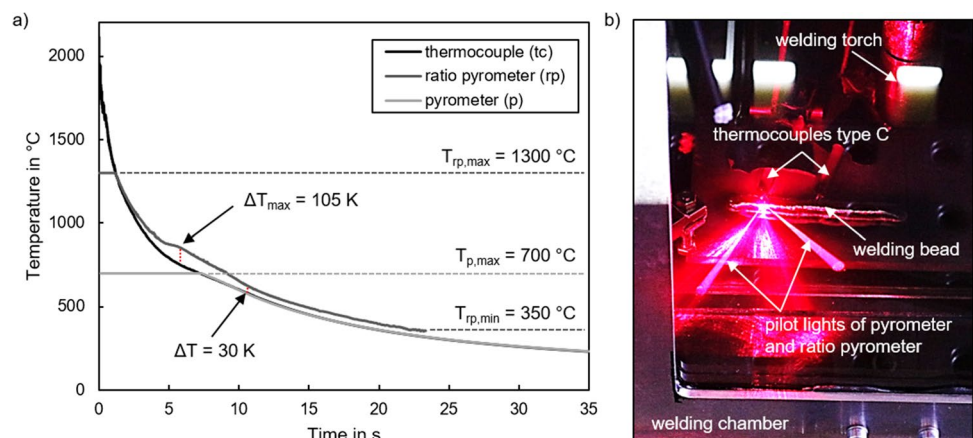


Fig. 6 a Schematic illustration of the temperature measurement setup for the experiments under variation of the structure width and interpass temperature (IPT) and **b** the measuring devices used as dependence of the interpass temperature for measuring the interpass temperature and for recording the cooling course (rp, ratio pyrometer; p, pyrometer)



3.3 Methods for characterization

The temperature measurement during the additive manufacturing process of the thick-walled structures was carried out by means of the experimental setup schematically shown in Fig. 5a. The measuring points of the pyrometers were rigidly connected to the handling system so that the measuring points are always located below the torch on the top layer of the structure.

Depending on the interpass temperature, one or two pyrometers were used. The distribution can be seen in Fig. 5b. In the case of an interpass temperature greater than 350 °C, the ratio pyrometer was used for process control (measurement of the IPT) and the cooling course. In the case of interpass temperatures lower than 350 °C, an additional pyrometer had to be used for the measurement of the interpass temperature and thus for the process control due to the limited measuring range of the ratio pyrometer.

Since the emission coefficient of the material to be measured has an influence on the optical temperature determination by means of single-wavelength pyrometers, the set emission coefficient was varied in test series and compared with the tactile temperature measurement by means of thermocouples and the ratio pyrometer.

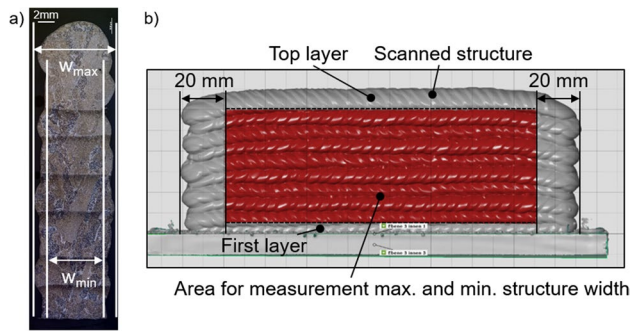


Fig. 7 **a** Display of the determined geometric parameters based on a cross-section and **b** methodology for determining the area for measuring the maximum and minimum structural widths using the example of a scanned wall structure

For the tests, the welding wire was focused with the optical measuring equipment and the pyrometers were positioned on one of the two pairs of thermocouples. The two thermocouples were placed in the welding path and welded over. The setup is shown in Fig. 6b. The temperature–time regime was recorded over the period of the welding process until cooling to a temperature of 100 °C, and the temperature curves were then compared. According to the diagram in Fig. 6a, it can be seen that the temperature curve of the partial radiation pyrometer, with a set emission coefficient of $\epsilon = 0.1$, agrees qualitatively and quantitatively with that of the thermocouple in the measurement range.

From the maximum temperature of 1300 up to approx. 1000 °C, the curves of the thermocouple and the ratio pyrometer match. Between 1000 and approx. 700 °C, there is a deviation of 105 K maximum. This is due to the transition of the surface of the weld metal from red-hot to shiny metallic and is accompanied by a different change in the emission value in the spectral ranges of the two pyrometers in the ratio pyrometer. Due to the measuring principle, this leads to the deviations shown. Below 700 °C, the temperature curves converge again with a constant difference of approx. 30 K between the thermocouple and

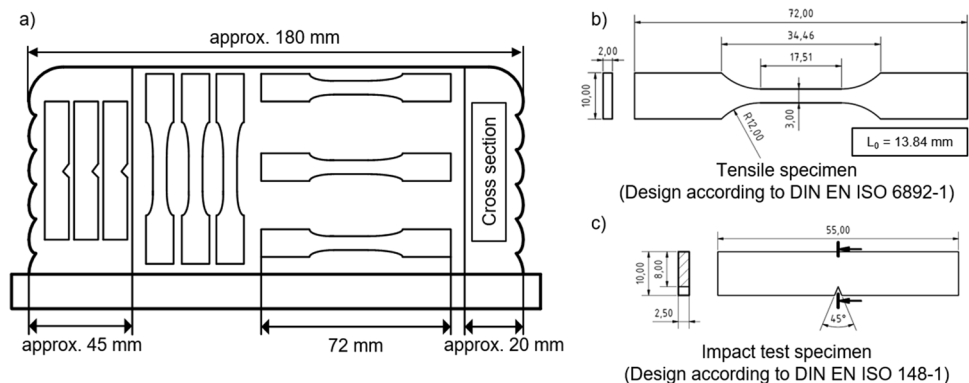
the ratio pyrometer. Accordingly, the qualitative curve is almost completely reproduced and allows the use of the ratio pyrometer for the comparative analysis of cooling times within the scope of the investigations.

The determination of the final contour proximity was carried out using a GOM Atos Core 300 3D scanner with a rotary table for specimen positioning. The generated 3D model of the specimen is subsequently analyzed with the associated software. For this purpose, a fitting plane according to Tschebyscheff is placed on the selected lateral surfaces of the structures (Fig. 7b). In this way, the maximum and minimum deviations of the opposing planes and thus the maximum and minimum structure widths can be determined. According to Eq. (2), the difference between maximum structure width w_{max} and minimum structure width w_{min} can be used to evaluate the near-net-shape. A difference as small as possible Δw corresponds to a high final contour closeness, since in this case the smallest amount of material must be subsequently removed in order to obtain the effectively usable structure width. Figure 7a illustrates the geometric quantities determined on the basis of a cross-section of a structure. For the measurement, both the first and the last layer as well as the edge areas of wall segments were excluded in order to avoid, for example, the influence of material accumulations at the start or end of the weld. Figure 7b illustrates the methodology using the example of a scanned wall structure.

$$\Delta w = w_{max} - w_{min} [\text{mm}] \quad (2)$$

In the final analysis step, the necessary machining was carried out to remove the specimens for metallographic and mechanical analysis as shown in Fig. 8a. To investigate the tensile strength R_m , specimens of shape *E* were designed according to the calculation specifications of DIN EN ISO 6892–1 for uniform strain specimens. Figure 8b shows the resulting tensile specimen dimensions. The tensile test was performed on a universal testing machine from Hegewald & Peschke Meß- und Prüftechnik GmbH, type inspect retrofit Zwick 1455, with a maximum tensile force of 25 kN.

Fig. 8 **a** Schematic illustration of the removal of the notched bar impact specimen (build-up direction) and the tensile specimen (build-up and welding direction) as well as the transverse section from the wall structures and representation of the geometry and dimensions for the tested **b** tensile specimens according to DIN EN ISO 6892–1 and **c** notched bar impact specimen according to DIN EN ISO 148–1



For the determination of the impact energy, undersize specimens were manufactured according to DIN EN ISO 148–1 with a V-notch. The dimensions of the specimens are shown in Fig. 8c. The impact energy was determined on an RKP 300 testing machine from Roell Amsler using a test hammer with an energy of 150 J.

The microstructural analysis of the produced welds was carried out by hardness measurements according to Vickers in accordance with DIN EN ISO 6507–1, using a hardness tester from Struers of type DuraScan 70 and an indenter with an indentation angle of 136° . The test force F was 9.81 N according to HV1. This enables the detection of local hardness variations that indicate different microstructures or compositions.

For the metallographic investigation, sections were first cut out of the specimen structures using a band saw with slow feed rate and high coolant flow. Subsequently, the specimens were mounted in epoxy resin (EpoxiCure2 cold embedding agent from Buehler) for improved handling. On a Buehler Phoenix 4000 V/2 sander, the specimens were coarsely and finely sanded with abrasive paper containing SiC particles with grit sizes 160, 320, and 2500. This was followed by a polishing process on discs with synthetic coating and additional suspensions to which 3- μm and 0.05- μm monocrystalline diamond particles were added. Visualization or contrasting of the microstructure was achieved by etching according to Kroll (50 ml distilled water, 40 ml nitric acid 65%, 10 ml hydrofluoric acid 40%) for approx. 15 to 45 s. The microstructure is examined using a Zeiss Discovery.V8 with an Axiocam 105 color and a Zeiss AX10 Scope.A1 with an Axiocam ICc3. The Discovery.V8 ($1\times-8\times$ magnification) allows examinations and panoramas over a large area of the sample. With the Zeiss AX10 and the Axiocam ICc3 camera used, the samples can be examined with a maximum magnification of $1000\times$. The specimen evaluation was performed with the Zeiss AxioVision software.

4 Results and discussion

4.1 Development of additive process strategies

4.1.1 Additive manufacturing of thin-walled structures

As a basis for the additive build-up process and the characterization of the energy-reduced, controlled short circuit, the achievable weld bead geometry was analyzed first. Figure 9 shows the weld bead width (a) and the weld bead height (b) as a function of the wire feed rate for varying welding speeds. The investigations were carried out using a wire diameter of $\varnothing_W = 1.0$ mm and the welding gas ArHe30. At wire feed rates lower than 6 m/min, no continuous weld

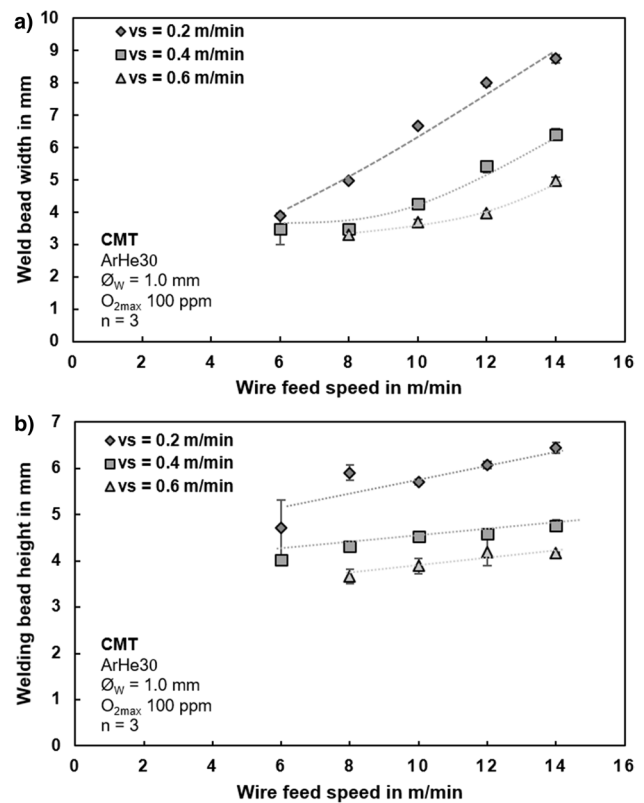


Fig. 9 a Weld bead width and b weld bead height as a function of wire feed speed v_W with variation of welding speed v_S (ArHe30, $\varnothing_W = 1.0$ mm)

beads could be generated regardless of the welding speed, which is why this range of values is not considered. The upper limit of the investigated wire feed speeds of 14 m/min is justified by the limitation of the short circuit process used in the power source. Maximum weld bead widths of $w = 8.8$ mm were produced at maximum wire feed of $v_W = 14$ m/min and lowest welding speed of $v_S = 0.2$ m/min. Minimum weld bead widths of $w = 3.4$ mm were obtained at the lowest wire feed rate of $v_W = 6$ m/min and the slowest welding speed of $v_S = 0.6$ m/min. Respectively, maximum and minimum weld bead heights of $h = 6.4$ mm and $h = 3.6$ mm were generated for the same input variables.

When considering the bead width, it increases with both an increase in wire feed and a reduction in welding speed. Furthermore, it can be seen that significantly higher bead widths were obtained with the lowest welding speed of 0.2 m/min compared to double or triple the welding speed. The difference between the bead widths at the welding speeds 0.4 m/min and 0.6 m/min is smaller.

With regard to the weld bead height, the same relationships can be identified. With increasing wire feed and reduced welding speed, the resulting bead height increases. However, the increase is smaller for the same increase in wire feed compared to the increase in bead width.

Based on the findings on the resulting weld bead geometries, thin-walled structures consisting of three layers were initially generated to determine suitable welding process influencing variables that enable a near-net-shape additive build-up. Depending on the energy input per unit length, different defect patterns occurred. At low energy inputs per unit length, interrupted weld beads were generated. This is caused either by an insufficient amount of molten material due to a wire feed speed that is too low in relation to the welding speed, or by a rapidly solidifying melt as a result of insufficient heat input. Due to its characteristic appearance, the defect pattern is called “humping.” In contrast, the weld metal sagged periodically at high line energies as a result of the high heat input and the increased melt pool volume with a simultaneous reduction in viscosity. Both phenomena negatively influence a near-net-shape additive build-up process or even prevent a build-up process. Figure 10 shows a schematic comparison of the defect patterns with the near-net-shape build-up, based on example images of generated structures and micrographs.

By forming the defect patterns, the range of suitable welding parameters is restricted when a single-row build-up strategy is applied. Figure 11 shows weld range diagrams by plotting the resulting energy per unit length as a function of wire feed and welding speed for the welding gases ArHe30 (Fig. 11a) and ArHe70 (Fig. 11b).

The value ranges of the occurrence of the collapsing melt and the humping are marked therein. It is evident that increasing the helium content in the shielding gas from 30 to 70% shifts the ranges of defect patterns to lower energy inputs per unit length. At the same time, the process window for a near-net-shape additive build-up process becomes smaller with the increase of the helium content. This results from the shift of the defect pattern of the collapsing melt to lower energy inputs per unit length compared to the shielding

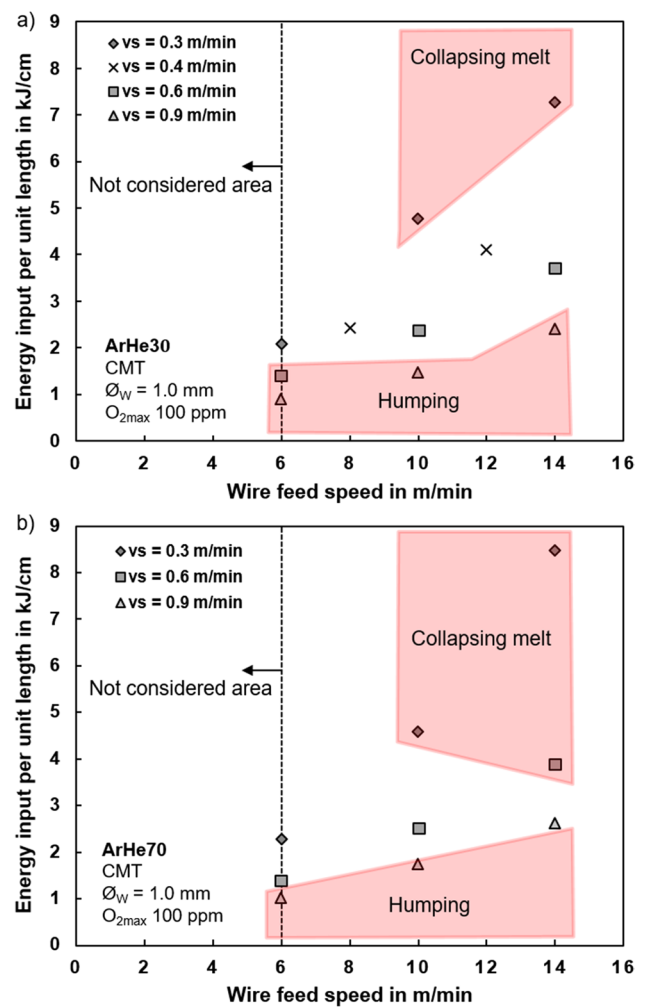


Fig. 11 Welding range diagrams with resulting energy input per unit length under variation of wire feed speed v_w and welding speed v_s using the welding gases (a) ArHe30 and (b) ArHe70

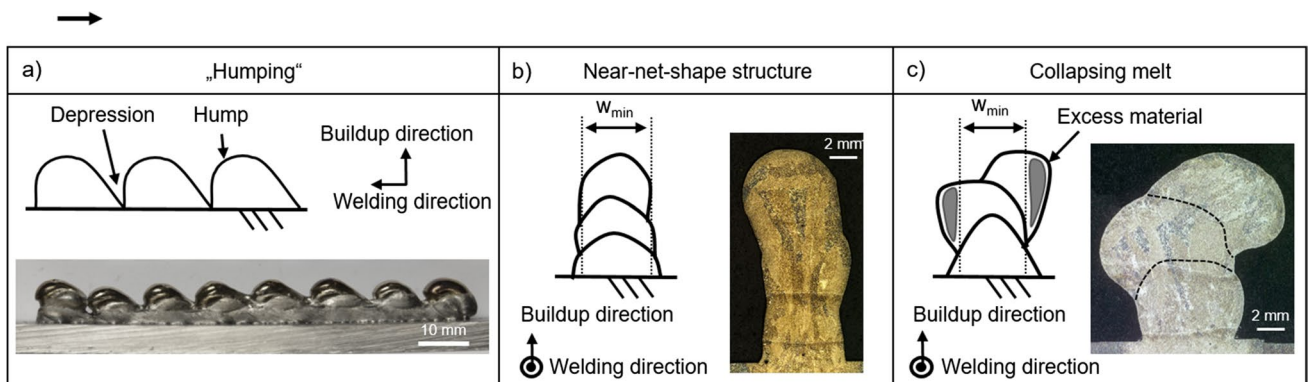


Fig. 10 Illustration of defect patterns (a and c) occurring during single-row additive manufacturing of thin-walled Ti-6Al-4 V structures by means of an energy-reduced, controlled short circuit in comparison to the near-net-shape build-up (b)

gas ArHe30. Consequently, with the shielding gas with the lower helium content, higher line energies and thus wider structures can be produced without the melt collapsing in the additive build-up process. The advantage of the shielding gas ArHe70 is nevertheless that the heat distribution in the arc is more homogeneous due to the higher helium content. The molten pool therefore has better wetting properties. This also shifts the occurrence of humping to lower energy inputs per unit length. This enables an additive build-up process with lower energy per unit length and smaller weld bead widths. As a result, structures with a smaller width can be produced compared to the shielding gas ArHe30. However, the results described refer only to the single-row build-up process.

For validation, one welding parameter set per shielding gas was selected within the defined process range and a single-row wall structure with a low structure width was built. A height corresponding to 30 layers was aimed for. Figure 12 shows the generated structures in side view (Fig. 12a and c) and top view (Fig. 12b and d), as well as the corresponding input and output parameters.

Using the inert gas ArHe30, a structure with a width of $w=4.77$ mm, a total height of $h_{\text{total}}=90.2$ mm, and a high final contour proximity could be generated. For this, an energy input per unit length of $E_S=2.16$ kJ/cm was determined, resulting from a wire feed speed of $v_W=6$ m/min, a welding speed of $v_S=0.3$ m/min, and a welding voltage of $U=15$ V.

Due to the higher helium content, it was possible to double the welding speed when using the shielding gas ArHe70 without producing an interrupted weld bead (no “humping”). This resulted in a lower energy input per unit length of $E_S=1.38$ kJ/cm and an increased welding voltage to $U=16.7$ V. The structure width is reduced to $w=4.09$ mm.

Due to the irregularity shown in Fig. 12c, the additive build-up process had to be stopped after 23 layers. This

results in a total height of approx. 41 mm. The irregularity in the layer build-up results from an increasing contact tip to work distance (CTWD) with increasing build-up height due to flatter layers. This led to a steady reduction in the welding voltage, an extinguishing of the arc, and thus ultimately to an abortion of the welding process. In conclusion, a constant check of the contact tip to work distance after generation of a defined number of layers is recommended and, if necessary, a manual adjustment of the build-up program is required.

4.1.2 Additive manufacturing of thick-walled structures

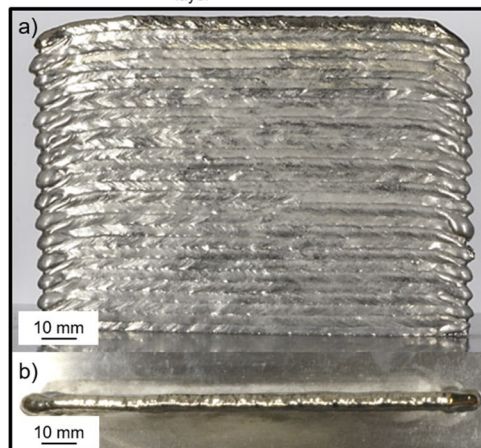
Overlaps of 10%, 20%, and 30% were used for the multi-row build-up strategy. The specifications are based on experience and publications from the field of steel processing using DED-Arc and specifically GMAW. According to Ding et al., this is about 26% [56]. The energy inputs per unit length used have a value of approx. 2.42 kJ/cm ($v_W=8$ m/min, $v_S=0.4$ m/min) and 4.1 kJ/cm ($v_W=12$ m/min, $v_S=0.4$ m/min). For each layer, four weld beads were placed next to each other for the lower energy input per unit length and three weld beads for the higher energy input per unit length. The sample with an overlap of 10% and $E_S=4.10$ kJ/cm is an exception here, since the addressed structure width could already be realized with two weld beads on the basis of the calculation.

The resulting structures are tabulated in the side view in Fig. 13. For the structures welded with the energy input per unit length of $E_S=2.42$ kJ/cm and with an overlap of 10% and 20%, a process termination occurred in the 8th and 4th layer, respectively, due to arc extinction. This is explained by the fact that no closed areas were generated, but the individual weld beads were placed next to each other with a poor connection. At the same time, the selected welding

Fig. 12 Generated thin-walled structures within the determined weld area with shielding gas **a**, **b** ArHe30 and **c**, **d** ArHe70 in **a**, **c** side and **b**, **d** top view

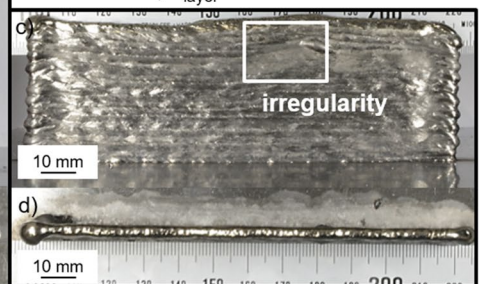
a), b): Shielding gas ArHe30

$E_S = 2.16$ kJ/cm; $v_W = 6$ m/min;
 $v_S = 0.3$ m/min; $U = 15$ V; $h_{\text{total}} = 90.2$ mm;
 $w = 4.77$ mm; $n_{\text{layer}} = 30$



c), d): Shielding gas ArHe70

$E_S = 1.38$ kJ/cm; $v_W = 6$ m/min;
 $v_S = 0.6$ m/min; $U = 16.7$ V; $h_{\text{total}} = 40.8$ mm;
 $w = 4.09$ mm; $n_{\text{layer}} = 23$



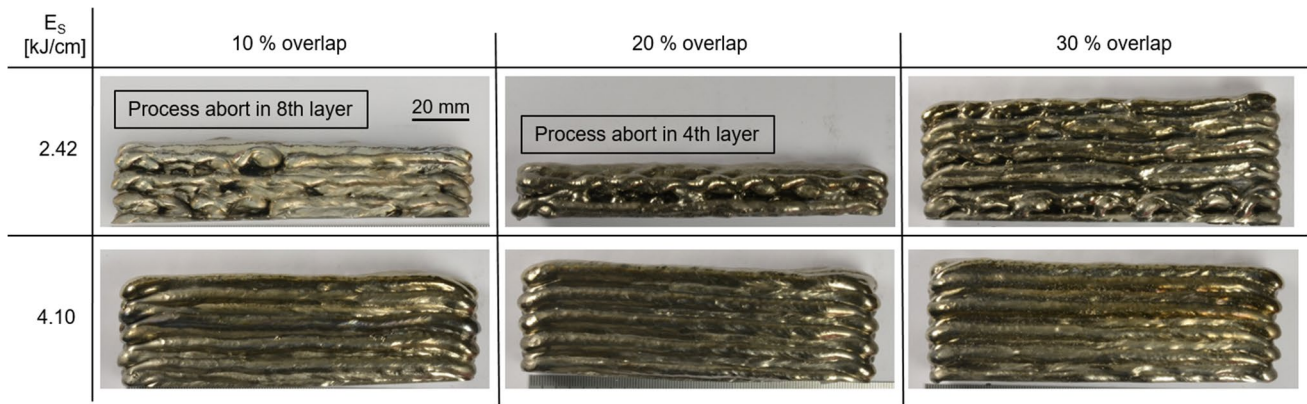


Fig. 13 Additively manufactured wall structures with multi-row build-up strategy under variation of the energy input per unit length and overlap in side view (10 layers, length = 120 mm)

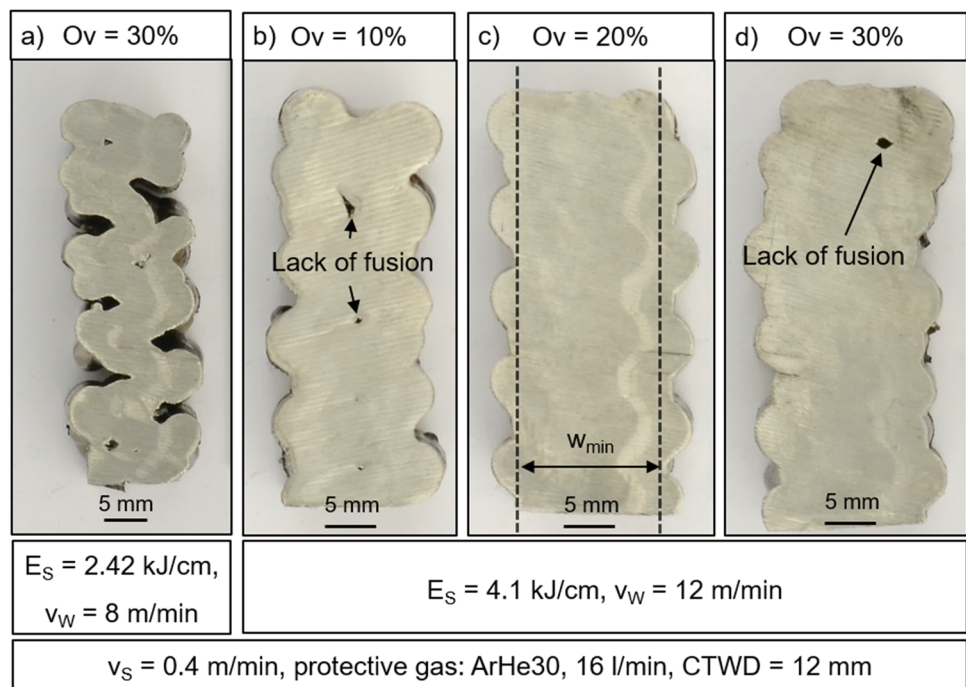
parameters formed narrow and super-elevated beads, which amplified the previously mentioned problem. The super-elevated weld beads can be described by a height-to-width ratio higher than 1.1. As a result, the arc partially burned on the adjacent weld bead of the same layer during the build-up process, due to cathode, due to the process-specific cathode spot wandering [26, 58]. This led to process instabilities and to an intensification of the irregularity of the layer surface, so that with increasing build-up height, the process instabilities occurred more frequently until the eventual process termination.

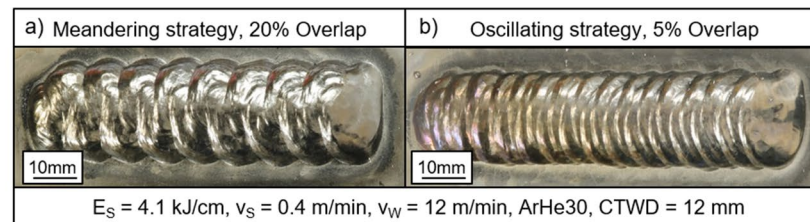
For the structure with an overlap of 30%, the build-up process of ten layers could be completed. This is due to the

fact that the larger overlap and the higher energy input cause the previously placed weld beads of a layer to fuse together more strongly and form a closed surface. In this case, the arc burns mainly on the underlying layer. Looking at the cross-section in Fig. 14a, it can be seen that the structure does not have a closed volume and thus no near-net-shape.

The structures welded with the energy input per unit length of $E_S = 4.10$ kJ/cm could be completely built up with the selected overlaps. The phenomenon of the arc jumping over to neighboring beads could not be observed. The arc burned exclusively on the underlying weld bead (Fig. 14 b-d). Closed layers were formed. This is due to the comparatively higher material and heat input, which favors

Fig. 14 Plot of cross-sections of wall structures and irregularities under variation of overlap and energy input per unit length for multi-row build-up strategy: (a) Ov = 30%, $E_S = 2.42$ kJ/cm; (b) Ov = 10%, $E_S = 4.10$ kJ/cm; (c) Ov = 20%, $E_S = 4.10$ kJ/cm; and (d) Ov = 30%, $E_S = 4.10$ kJ/cm (CTWD—contact tip to work distance)





c)	Meandering strategy Welding gas: ArHe30	Meandering strategy Welding gas: ArHe70	Oscillating strategy Welding gas: ArHe30	Oscillating strategy Welding gas: ArHe70
Wall structures (side view) 10 mm				
Minimum width [mm]	19.36	21.34	18.16	20.53
Maximum width [mm]	26.05	26.82	26.08	27.04
Δ -width [mm]	6.69 ($\approx 26\%$)	5.48 ($\approx 21\%$)	7.92 ($\approx 30\%$)	6.51 ($\approx 24\%$)
average height [mm]	34.3	33.1	44.3	40.5
Area of minimum width [mm ²]	664.96	706.89	805.85	831.5

Fig. 15 Display of the single-layer weld beads with the overlaps selected for the additive build-up of (a) $Ov=20\%$ for the meander and (b) $Ov=5\%$ for the oscillating strategy and c comparison of the wall structures generated using the meander ($Ov=20\%$) and oscillating ($Ov=5\%$) strategies with variation of the welding gas used (ArHe30 and ArHe70) with respect to geometrical properties after generation of a digital model by means of optical 3D measurement technology

the fusion of the beads together. At the same time, the height-to-width ratio of the weld beads formed is approx. 1.0 and, accordingly, the beads are not super-elevated, in contrast to the weld beads of the previously used energy input per unit length. This also favors good bonding of the weld beads to each other. However, these structures are again characterized by a strong waviness of the lateral surface. For visual inspection of the bonding, the cross-sections are shown in Fig. 14b, c, and d.

It can be seen that the high viscosity of the melt pool and the associated displacement of the melt lead to the increased occurrence of bonding defects and a reduction in the near-net-shape. Bonding defects can be seen in the structure with an overlap of 10% as well as at 30%. In the cross-section of the structure with an overlap of 20%, no bonding defects are evident. However, the quality of the side surfaces is poor, since a periodically changing deflection of the melt per layer can be seen. This significantly reduces the usable minimum structure width w_{min} .

In summary, the multi-row or parallel build-up strategy widely used in the additive processing of steels, in which individual weld beads are placed next to each other with a defined overlap, proved to be unsuitable for the near-net-shape additive build-up of thick-walled structures for the material Ti-6Al-4 V using an energy-reduced, controlled short circuit.

In contrast, both the meandering and the oscillating welding patterns proved to be suitable, since

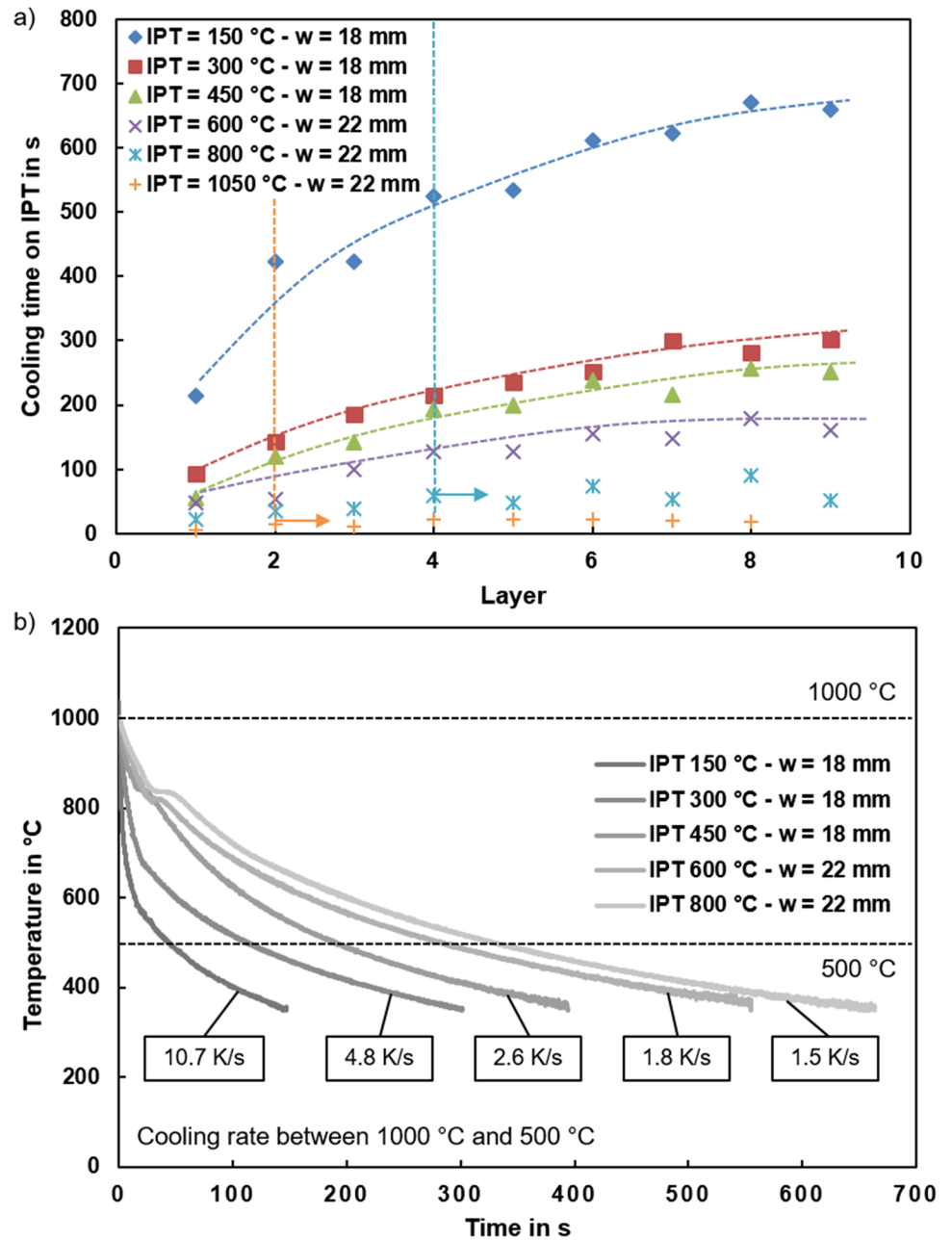
near-net-shape structures could be produced without the occurrence of bonding defects. In the course of the investigations, the overlap between the sub-segments and subsequently the shielding gas of the welding process was varied between ArHe30 and ArHe70 under constant energy input per unit length of $E_s = 4.10$ kJ/cm, and the influence on the final contour proximity was evaluated. In the first step, a single-layer weld bead was welded while varying the overlap. A structure width of $w = 22$ mm was addressed. The weld structure was then visually evaluated using the following qualitative evaluation criteria:

- Uniformity of the structure edge
- Uniformity of the structure surface
- Flatness of the structure

The overlaps used to generate the wall structures are shown with a photograph of the respective single-layer structures as a function of the build-up strategy in Fig. 15a and b.

The 7-layer wall structures generated using the specified welding parameters are shown in Fig. 15c. In addition, the geometric properties determined from the 3D scan are also listed. For the shielding gas ArHe30, the usable or effective structure width, starting from the maximum structure width, decreased by 26% for the meander strategy and by 30% for the oscillating strategy. Increasing the helium content in the shielding gas from 30 to 70%

Fig. 16 Illustration of (a) the cooling time on IPT as a function of the layer or rather the build-up height for the different interpass temperatures and structure widths and (b) the temperature–time curves of the last layer with variation of the interpass temperature or structure width and representation of the cooling rates between 1000 and 500 °C

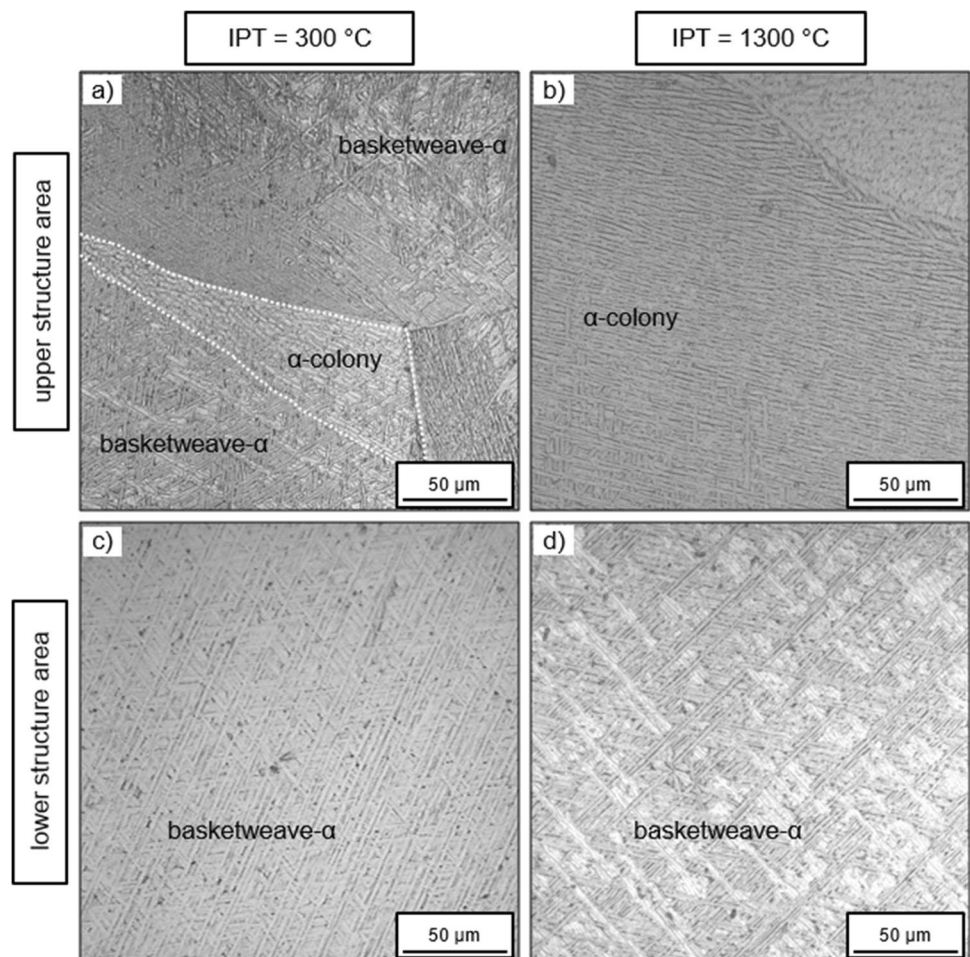


resulted in an increase in the near-net-shape by reducing the deviation between maximum and minimum structure width to 21% for the meander strategy and to 24% for the oscillating strategy.

Accordingly, it should be noted that the use of a shielding gas composition with a higher helium content can reduce the difference between maximum and minimum structure width and thus improve the near-net-shape. A comparison of the build-up strategies shows a larger resulting height of the structure. This is due to the larger material input in the oscillating strategy, due to a

longer weld path despite a smaller overlap. This results from the definition of the overlap. On a structure length of 10 mm, the weld path length of the meander strategy is only about 73% of the weld path length of the oscillating strategy.

Fig. 17 Light microscopic images of the characteristic lamellar microstructure of cross-sections in the upper regions (a, b) and lower regions (c, d) of the structures with the interlayer temperatures of 300 °C (a, c) and 1300 °C (b, d)



4.2 Development of additive process strategies

4.2.1 Analysis of the interpass temperature on the build-up and cooling process

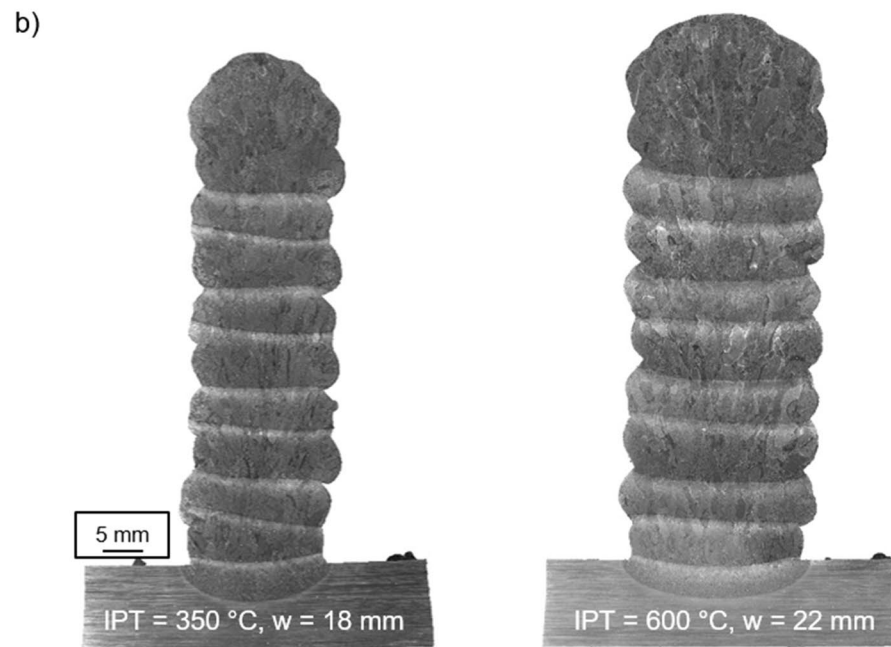
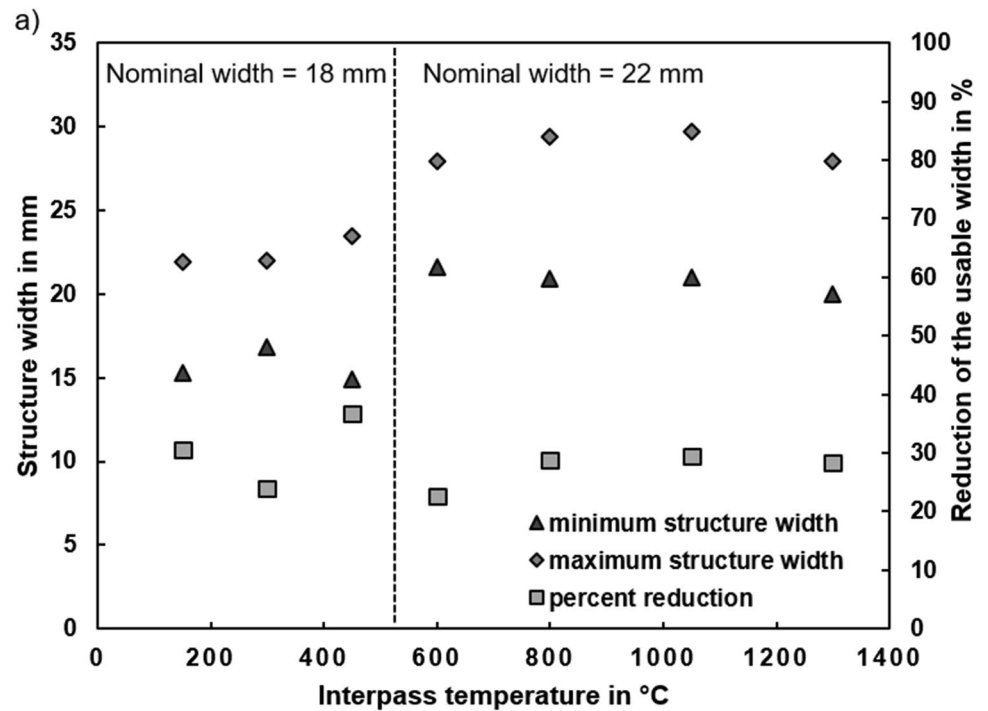
Looking at the cooling time to interpass temperature after the layer build-up in Fig. 16a, it can be seen that increasing the interpass temperature reduces the time required in the cooling process. There is a significant difference between the values for IPT of 150 °C and 300 °C. If the IPT is increased further, the reduction in the cooling time to interpass temperature per layer becomes less.

Regardless of the interpass temperature, the cooling time increases with increasing number of layers. This is due to the steady increase in thermal energy as a result of the continuous energy input during layer generation. Accordingly, lower temperature gradients within the structure result in limiting heat removal and result in lower cooling rates. Nevertheless, a decrease in the increase of the values per layer can be observed. The magnitude of the decrease in the increase depends on the interpass temperature. This saturation range, in which there is no further increase in the cooling time

between the individual layers, is comparable to a quasi-stationary state. This describes a process state in which the thermal energy supplied and the thermal energy dissipated within a layer in the structure are close to equilibrium. Comparable cooling rates are equivalent to homogeneous microstructure formation and correspondingly homogeneous mechanical properties. For the high interpass temperatures of 800 °C and 1050 °C, this is already achieved after the 4th and the 2nd layer, respectively, as a result of the heat build-up. At an interpass temperature of 600 °C, a slight increase in the values is still evident. In summary, it can be said that with an increase in the interpass temperature, the quasi-stationary range is reached earlier in the additive build-up process or after a lower number of welded layers. It remains to be clarified to what extent the achievement of the quasi-stationary state correlates with the formation of homogeneous properties.

Figure 16b shows the cooling curves of the last layers of the specimens. As the interpass temperature increases, the curves converge closer to each other. This also leads to a flattening of the curves and a slower cooling rate. This behavior suggests that heat builds up in the specimens as

Fig. 18 a Comparison of maximum and minimum structure width and percentage reduction of structure width as a function of the IPT for the addressed structure widths and **b** plot of the cross-sections of the specimen with the highest near-net-shape



the interpass temperature increases. The heat accumulation then also causes the cooling rate to slow down. In addition, the corresponding cooling rate for the range 1000–500 °C is noted.

Over this temperature range, the formation of the α -titanium lattice occurs. The cooling rates vary between 10.7 K/s at an interlayer temperature of 150 °C and 1.5 K/s at the interlayer temperature of 800 °C. According to Liu et al. in this range of cooling rates, the

β -titanium transforms into a lamellar microstructure with basketweave- α (Widmanstätten- α) and α -colonies, without the formation of massive α -titanium or martensite [2]. In addition to the formation of grain boundary- α , these two microstructures dominate the microstructure of the manufactured specimens, regardless of the selected interpass temperatures. The different microstructures can be seen in Fig. 17 for two different structure ranges and interpass temperatures. Nevertheless, the lamellar microstructures form differently

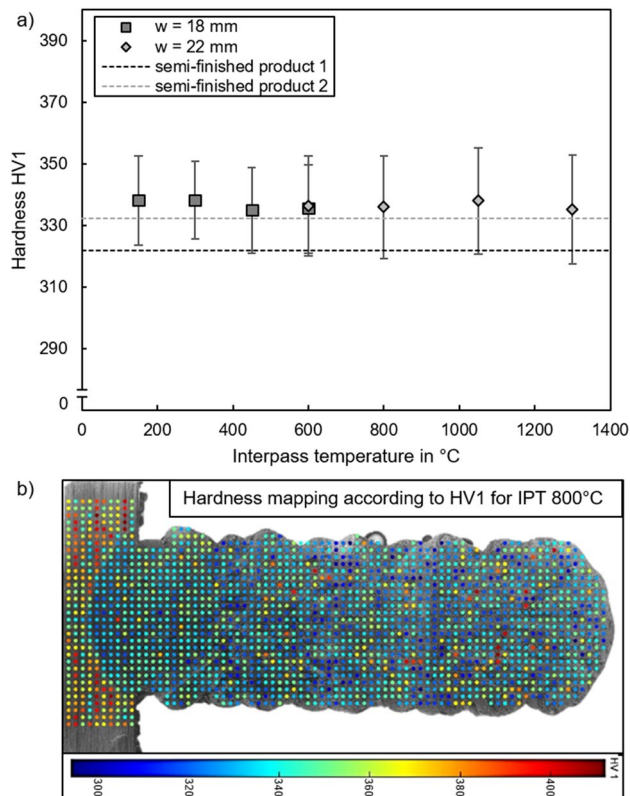


Fig. 19 **a** Resulting average hardness values according to HV1 as a function of the interpass temperature for the additive structure, the heat-affected zone in the substrate and the unaffected semifinished product as a reference in the surface and cross-sections, and **b** hardness mapping according to HV1 with a distance of the measuring points of 1 mm in the cross-section of the sample structure with an interpass temperature of 800 °C

depending on the build-up height and the interpass temperature. This is due to the different resulting cooling rates as a result of varying amounts of accumulated heat in the structure and thus different steep temperature gradients. With a comparatively high cooling rate at a low build-up height or a low selected interpass temperature, fine lamellar structures of completely or mainly basketweave- α are initially formed. At low cooling rates, for example at a high build-up height or high interpass temperatures, the lamellar structure becomes more coarse-grained and proportionally more α -colonies are formed [21]. At the same time, the heat cycles cause further coarsening of the grain structure due to additional welded layers being applied. Accordingly, a coarse microstructure can also be found in lower structural areas, but here, the proportion of basketweave- α is usually greater as a result of initially faster cooling from the β -range (Fig. 17c, d).

The decrease in cooling rates, as previously mentioned, suggests the formation of a heat build-up, which is more pronounced with a higher interpass temperature. Accordingly, with a higher interpass temperature, the

component can be generated in a shorter time, but the material cools slower due to lower temperature gradients. The same behavior of the approximation of the cooling curves as shown in Fig. 16b is evident within a specimen with increasing number of layers or build-up height. In the first layer, a cooling rate of 15.3 K/s is present. In layer four, there is a quasi-static value of 3.5 K/s with the implication of a heat build-up which, however, is in equilibrium here. In connection with the microstructure, this would indicate that the mechanical properties must be the same from layer four up to the top layer. There is then a difference to layers one to three.

4.2.2 Characterization of selected resulting geometrical and mechanical properties

To analyze the resulting near-net-shape, the maximum and minimum structure widths determined by using a 3D model and the percentage deviation between the values (expressed by the reduction of the usable width) as a function of the interpass temperature were plotted in Fig. 18a.

Here, no systematic correlation between the final contour proximity (expressed by the minimum deviation between minimum and maximum structure width) is apparent. The structures shown in Fig. 18b in cross-section exhibited the smallest deviations of -23% and -22.5% at an interpass temperature of 300 °C for the 18-mm wide structure and at an interpass temperature of 600 °C for the 22-mm wide structure.

For the analysis of the resulting mechanical properties, the resulting average hardness according to HV1 as a function of the interpass temperature used is first shown in Fig. 19a. Furthermore, hardness values for the unaffected substrate material (semifinished product) in cross-section and surface section are listed for comparison as a reference. Irrespective of the interpass temperature, the structures have a mean hardness value of approx. 336 HV1 and are within the range of variation from one another with a mean standard deviation of 15 HV1. At the same time, the determined hardness values are almost in the average value range, which is given in the literature as 300–400 HV for the alloy Ti-6Al-4 V [59]. The results are also consistent with previous studies regarding the insignificant effect of the passed temperature regime on the resulting component hardness in additive manufacturing with DED-Arc. Here, the hardness values vary between 290 HV und 350 HV0.5 [9, 21, 32, 34].

The substrate is at an average hardness of 321 HV1 and 330 HV1 in the different directions of observation of the cross-section and surface section, respectively. Thus, the inhomogeneity in the hardness values between the surface and cross-sections in the unaffected semifinished product is greater than the difference between the hardness values of the additive structures generated with different interpass temperatures. Due to the superficially different cooling

Fig. 20 Optical microscope images of Ti-6Al-4 V microstructure from a heat unaffected semifinished product and from the bottom of the substrate to the first layer of the additive structure (a) banded, fully equiaxed microstructure with α -grains (white) and intergranular β at grain boundaries of the unaffected semifinished product, (b) fine bimodal microstructure with α -grains (white) and into the prior β -grains transformed microstructure of the substrate below the heat-affected zone (HAZ), (c) coarsened bimodal microstructure with less equiaxed and more lamellar α -grains in the HAZ, and (d) fully, coarsened lamellar microstructure in the remelted zone of the first layer

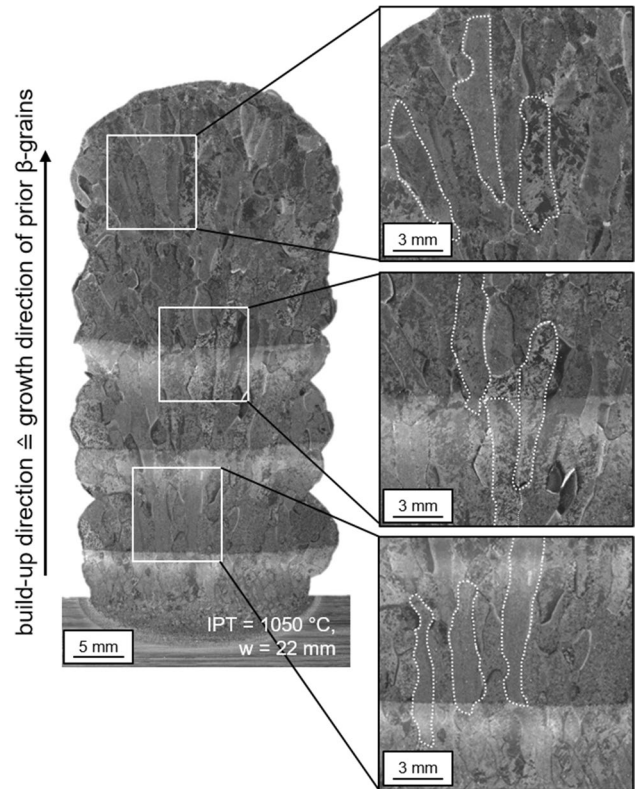
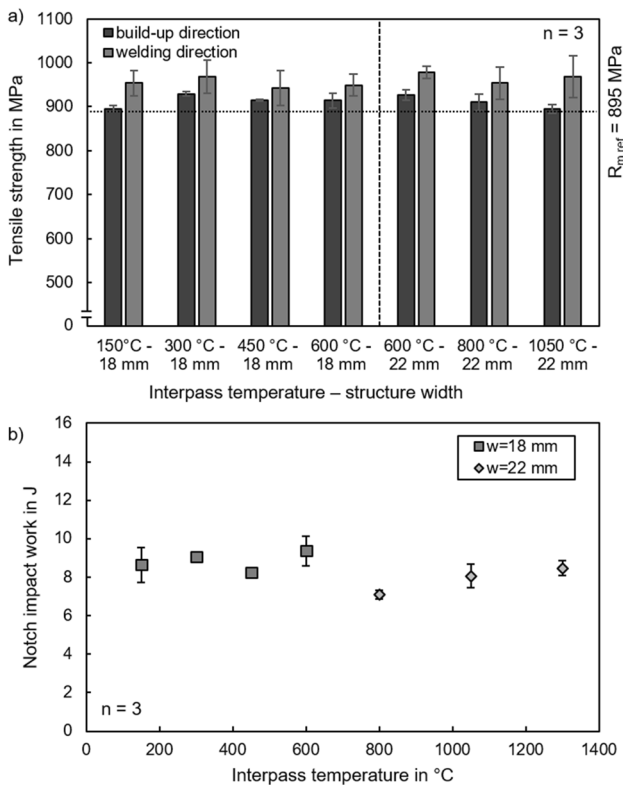
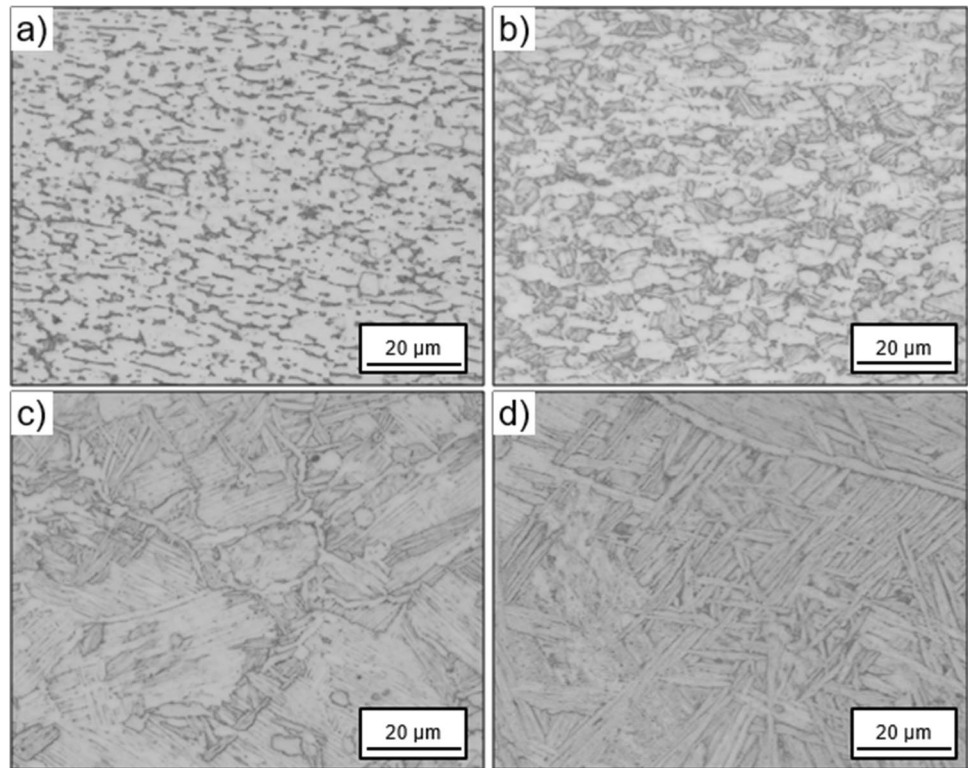


Fig. 21 a Tensile strength as a function of interpass temperature and structure width for the specimens taken in the build-up and welding directions, and b the impact energy as a function of interpass temperature and structure width

Fig. 22 Illustration of the strongly lamellar growth of the coarse prior β -grains in the build-up direction based on an optical microscope image of a cross-section with detailed images of the microstructure and exemplary outlining of prior β -grains

processes of the specimens, which however do not result in any difference in the hardness measurement, it is concluded that the process-related heat treatment is comparable despite different boundary conditions (interpass temperature) and therefore results in the formation of comparable microstructures and material properties. For this to happen, at least two zones with different cooling behavior must form. In the surface-near edge zone, the varying cooling behavior is measured by means of the pyrometer, but this only applies to a small area in terms of volume. The area within the structure exhibits comparable cooling behavior and the corresponding heat treatment for all specimens. The result is the same hardness, regardless of the interpass temperature.

Figure 19b illustrates the differences by showing the hardness mapping of the transverse section of the specimen with an interpass temperature of 800 °C. At the same time, the color-coded representation of the individual measuring points shows that there is no conspicuous distribution or accumulation of hardness values in the structure, which could be determined by varying temperature–time regimes during the additive build-up process with a constant interpass temperature. Below the heat-affected zone (HAZ), hardening is evident in the substrate, which is likely due to the heat-induced recrystallization of the formerly banded, equiaxed microstructure of the semifinished product (Fig. 20a) to a fine bimodal microstructure (Fig. 20b) [50]. This microstructure of the substrate is significantly finer compared to the coarsened bimodal microstructure in the HAZ (Fig. 20c) or the fully lamellar, coarsened microstructure of the remelted zone in the first layer in the additive structure (Fig. 20d) and also has a characteristically higher hardness than the equiaxed or lamellar microstructure [60, 61]. This results in a mean hardness of approx. 356 HV1, which is approx. 20 HV1 higher than the hardness of the additive structure, which almost completely exhibits a lamellar microstructure mainly consisting of fine and coarse α -colonies and Widmanstätten- α .

Figure 21a shows the tensile strengths achieved by the test specimens. Again, no systematic correlation was found between the tensile strength and the interpass temperature used. The same applies to the increase in the structure width from 18 to 22 mm and the associated increase in the energy input per layer from 369 to 508 kJ. Tensile strength values range from 895 to 980 MPa, which is within the average of previously determined tensile strengths for DED-Arc, which vary from 852 to 1033 MPa [8, 15, 22, 23, 25, 32, 40, 46].

All specimens thus meet the minimum tensile strength value for the pure weld metal of 895 MPa specified by the wire manufacturer. Thus, the findings are in line with the investigations of Lu, who also found no significant influence of the interpass temperature on the tensile strength and was able to determine values between 850 and 910 MPa. However, the interpass temperature was limited to a maximum of 300 °C as a result of beginning oxidation processes [34].

The tensile strengths are also almost in the identical range that was measured by Vazquez et al. (895–995 MPa) [35]. However, the results shown here do not show the relation that with an increase of the cooling rate and thus a finer resulting microstructure, the tensile strength is significantly increased from 895 to 995 MPa. The difference in the experimental procedure is that Vazquez et al. used a time-controlled build-up process and in this study a temperature-controlled build-up process was used.

The deviation between the specimen in build-up and welding direction is comparatively small, with a maximum difference of approx. 7% when the overlapping scattering areas are also considered. The systematic difference results from an anisotropy of the microstructure. Due to the cyclic remelting of the lower layers during the application of the top layer, the grains grow over several layers. This results in a strongly lamellar microstructure in the center of the structure and the grains partially grow over more than half of the structure. The lamellar growth of the prior β -grains is exemplified in Fig. 22 by the white lines drawn on a transverse section of a structure.

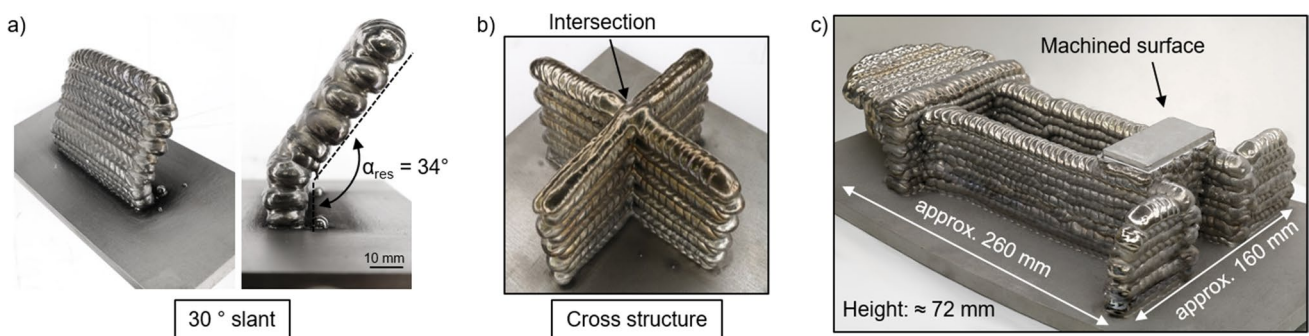


Fig. 23 a Additively manufactured bevels by means of neutral torch holding (0°) made of Ti-6Al-4 V with an addressed bevel angle of 30°, b build-up of a circular structure under variation of the meander

width, and c demonstrator component with partially machined surface (milled) and the dimensions 260 mm × 160 mm × 72 mm (L × W × H)

Accordingly, in build-up direction, there are fewer grain boundaries at which the dislocation movements can accumulate. The highly lamellar grains are parallel to the tensile axis in the build-up direction. As a result, the tensile strength values are slightly lower. In the welding direction, the strongly lamellar grains are not parallel to the tensile axis, but rotated by 90° to it. Therefore, comparatively more grain boundaries are located in the tensile direction, where dislocation movements can accumulate. Accordingly, higher tensile strength values are measured. The results obtained are in agreement with a large number of previous studies [8, 15, 21–23, 46, 62]. In summary, it can be concluded that the interpass temperature in the investigated value range between 150 and 1050 °C has a subordinate influence on the resulting tensile strength.

With regard to the fracture behavior under impact loading, no systematic correlation to the interpass temperature or the structure width could be established on the basis of the notched bar impact work. The results of the notched bar impact test can be seen in Fig. 21b. Values of maximum $W=9.4$ J for the interpass temperature of 600 °C (18 mm width) and minimum $W=7.1$ J for the interpass temperature of 800 °C (22 mm width) were determined. Brittle fracture behavior is present. The fracture surfaces of the specimens exhibit the characteristic appearance of a separation fracture. Accordingly, the coarsening of the microstructure and especially of the grain boundary- α , which is observed with increased interpass temperature, does not seem to have a significant influence on the notched bar impact energy. This is in contrast to the elongation at break. In several studies, an increase in heat input or a decrease in weld pause time or an increase in interpass temperature was associated with an increase in the thickness of grain boundary- α and with a decrease in elongation at break [15, 35]. The reasons for the absence of this relation are part of future investigations.

In summary, it can be concluded that the interpass temperature and the temperature–time regime passed during the additive build-up of the thick-walled structures have a minor influence on the resulting geometrical and mechanical properties, such as near-net-shape or tensile strength.

4.3 Transfer of the results to demonstrator components

In the final step of the investigations, the knowledge gained was transferred to 3D structures, such as the production of bevels with a neutral torch position (0°). Here, using the meander strategy, resulting angles of up to 30° could be produced with a good near-net-shape without additional torch adjustment, as shown in Fig. 23a. The

resulting angle deviation between nominal and actual was a maximum of 4°.

In a further step, web crossings were mapped by welding a cross-structure. This is shown in Fig. 23b. In order to avoid connection problems caused by an extinguishing and restarting arc in the area of the intersection, a special path strategy was used. Here, the meander direction was not varied independently of the individual sub-segments of the cross within a layer; instead, the meander width was varied in the crossing structural areas. A 90° rotation of the meander direction was performed layer by layer to compensate for any variations in the structure height due to the width variation. The cross-structure could be generated over the desired structure height without interruption. At the same time, a complete connection has been achieved in the area of the crossing point.

Furthermore, a demonstrator component, as shown in Fig. 23c, was built. This is the unmachined contour of a latch, which is used in the aviation industry, with a weight of approx. 2.8 kg. The demonstrator part includes a variety of challenging aspects, such as overhangs, slopes, or crossings. The assembly was carried out in two subassemblies, with an adjustment by a turn-tilt table. For the assembly, the structure was divided into individual segments, which were mapped using the meander strategy. In the case of a width variation in the structure, the meander direction was rotated by 90°. A rotation of the meander direction was performed if the meander width was greater than the sub-segment length.

5 Conclusion

The investigations carried out have provided extensive knowledge on the additive manufacturing of components made of Ti-6Al-4 V by means of the GMAW welding process with regard to suitable build-up strategies and the influence of the temperature–time regime on the resulting part properties.

The following findings can be listed:

- Fundamental investigations into the process of the energy-reduced, controlled short circuiting with reversing wire movement have resulted in welding range diagrams for different shielding gas compositions, which enable the additive build-up of near-net-shaped, thin-walled structures. In this context, it was possible to evaluate defect patterns that occur outside the shown suitable welding range. The usage of these parameters either leads to an end of the additive build-up process due to collapsing melt or the occurrence of humping, or reduces the economic efficiency due to a significant reduction of the near-net-shape.
- For the generation of near-net-shape and defect-free thick-walled structures, build-up strategies and charac-

teristic parameters such as overlap or energy input were varied. Both the meandering and the oscillating build-up strategies were found to be suitable.

- During the additive manufacturing process, the temperature regime was specifically influenced by varying the interpass temperature and selected geometrical and mechanical properties were investigated. It was shown that the interpass temperature has a minor influence on tensile strength, notched bar impact energy, and hardness. This legitimizes the increase of the interpass temperature to reduce the necessary build-up time. The specifications of the wire manufacturer regarding the minimum tensile strength of 895 MPa were exceeded regardless of the interpass temperature or the structure width. This results in an increase of the economic efficiency for the additive manufacturing of components made of Ti-6Al-4 V.
- Regardless of the selected interpass temperature, the tensile specimens exhibited tensile strengths about 7 MPa higher when taken in the welding direction as opposed to the build-up direction. This results from the pronounced lamellar grain growth of the prior β -grains in the build-up direction.

Funding Open Access funding enabled and organized by Projekt DEAL. The IGF Project No. 20483 BR/DVS-Nr.: 13.1009 of the research association, “Schweißen und verwandte Verfahren e.V.” of the DVS, Aachener Straße 172, 40223 Düsseldorf, was on the basis of a resolution of the German Bundestag, promoted by the Federal Ministry for Economic Affairs and Energy via AiF within the framework of the program for the promotion of joint industrial research and development (IGF). The authors thank all the industrial participants for funding and support.

Declarations

Conflict of interest The authors declare no competing interests.

Open Access This article is licensed under a Creative Commons Attribution 4.0 International License, which permits use, sharing, adaptation, distribution and reproduction in any medium or format, as long as you give appropriate credit to the original author(s) and the source, provide a link to the Creative Commons licence, and indicate if changes were made. The images or other third party material in this article are included in the article's Creative Commons licence, unless indicated otherwise in a credit line to the material. If material is not included in the article's Creative Commons licence and your intended use is not permitted by statutory regulation or exceeds the permitted use, you will need to obtain permission directly from the copyright holder. To view a copy of this licence, visit <http://creativecommons.org/licenses/by/4.0/>.

References

1. Giglio M, Manes A, Viganò F (2012) Ductile fracture locus of Ti-6Al-4V titanium alloy. *Int J Mech Sci* 54(1):121–135
2. Liu S, Shin YC (2019) Additive manufacturing of Ti6Al4V alloy: a review. *Mater Des* 164:107552
3. Ding D, Pan Z, Cuiuri D, Li H (2015) Wire-feed additive manufacturing of metal components: technologies, developments and future interests. *Int J Adv Manuf Technol* 81(1–4):465–481
4. Wei HL, Bhadeshia HKDH, David SA, DebRoy T (2019) Harnessing the scientific synergy of welding and additive manufacturing. *Sci Technol Weld Joining* 24(5):361–366
5. Mi G, Wei Y, Zhan X, Gu C, Yu F (2014) A coupled thermal and metallurgical model for welding simulation of Ti-6Al-4V alloy. *J Mater Process Technol* 214(11):2434–2443
6. Wu B, Pan Z, Ding D, Cuiuri D, Li H (2018) Effects of heat accumulation on microstructure and mechanical properties of Ti6Al4V alloy deposited by wire arc additive manufacturing. *Addit Manuf* 23:151–160
7. Da Silva LJ, Souza DM, de Araújo DB, Reis RP, Scotti A (2020) Concept and validation of an active cooling technique to mitigate heat accumulation in WAAM. *Int J Adv Manuf Technol* 107(5–6):2513–2523
8. Wang F, Williams S, Colegrove P, Antonysamy AA (2013) Microstructure and mechanical properties of wire and arc additive manufactured Ti-6Al-4V. *Metall and Mat Trans A* 44(2):968–977
9. Wang J, Lin X, Li J, Hu Y, Zhou Y, Wang C et al (2019) Effects of deposition strategies on macro/microstructure and mechanical properties of wire and arc additive manufactured Ti 6Al 4V. *Mater Sci Eng, A* 754:735–749
10. Wang J, Lin X, Wang J, Yang H, Zhou Y, Wang C et al (2018) Grain morphology evolution and texture characterization of wire and arc additive manufactured Ti-6Al-4V. *J Alloy Compd* 768:97–113
11. Xie Y, Gao M, Wang F, Zhang C, Hao K, Wang H et al (2018) Anisotropy of fatigue crack growth in wire arc additive manufactured Ti-6Al-4V. *Mater Sci Eng, A* 709:265–269
12. Zhang X, Martina F, Ding J, Wang X, Williams SW (2017) Fracture toughness and fatigue crack growth rate properties in wire + arc additive manufactured Ti-6Al-4V. *Fatigue Fract Engng Mater Struct* 40(5):790–803
13. Yi H-J, Kim J-W, Kim Y-L, Shin S (2020) Effects of cooling rate on the microstructure and tensile properties of wire-arc additive manufactured Ti-6Al-4V alloy. *Met Mater Int* 26(8):1235–1246
14. Ho A, Zhao H, Fellowes JW, Martina F, Davis AE, Prangnell PB (2019) On the origin of microstructural banding in Ti-6Al4V wire-arc based high deposition rate additive manufacturing. *Acta Mater* 166:306–323
15. Baufeld B, van der Biest O, Gault R (2010) Additive manufacturing of Ti-6Al-4V components by shaped metal deposition: microstructure and mechanical properties. *Mater Des* 31:S106–S111
16. Benakis M, Costanzo D, Patran A (2020) Current mode effects on weld bead geometry and heat affected zone in pulsed wire arc additive manufacturing of Ti-6-4 and Inconel 718. *J Manuf Process* 60:61–74
17. Fu J, Qiu K, Gong L, Liu C, Wu Q, Lu J et al (2017) Effect of tool-path on morphology and mechanical properties of Ti-6Al-4V fabricated by wire and arc additive manufacturing. *MATEC Web Conf* 128:5009
18. Raguvvarun K, Balasubramaniam K, Rajagopal P, Palanisamy S, Nagarajah R, Hoye N et al (2015) A study of internal structure in components made by additive manufacturing process using 3 D X-ray tomography. *AIP Conference Proceedings* 1650:146
19. Lin JJ, Lv YH, Liu YX, Xu BS, Sun Z, Li ZG et al (2016) Microstructural evolution and mechanical properties of Ti-6Al-4V wall deposited by pulsed plasma arc additive manufacturing. *Mater Des* 102:30–40
20. Lin J, Lv Y, Liu Y, Sun Z, Wang K, Li Z et al (2017) Microstructural evolution and mechanical property of Ti-6Al-4V wall deposited by

- continuous plasma arc additive manufacturing without post heat treatment. *J Mech Behav Biomed Mater* 69:19–29
21. Xian G, Jm Oh, Lee J, Cho SM, Yeom J-T, Choi Y et al (2022) Effect of heat input on microstructure and mechanical property of wire-arc additive manufactured Ti-6Al-4V alloy. *Weld World* 66(5):847–61
 22. Baufeld B, Brandl E, van der Biest O (2011) Wire based additive layer manufacturing: comparison of microstructure and mechanical properties of Ti-6Al-4V components fabricated by laser-beam deposition and shaped metal deposition. *J Mater Process Technol* 211(6):1146–1158
 23. Brandl E, Baufeld B, Leyens C, Gault R (2010) Additive manufactured Ti-6Al-4V using welding wire: comparison of laser and arc beam deposition and evaluation with respect to aerospace material specifications. *Phys Procedia* 5:595–606
 24. Almeida PS, Williams S (2010) Innovative process model of Ti-6Al-4V additive layer manufacturing using cold metal transfer (CMT). 2010 International solid freeform fabrication symposium
 25. Taberner I, Paskual A, Álvarez P, Suárez A (2018) Study on arc welding processes for high deposition rate additive manufacturing. *Procedia CIRP* 68:358–62
 26. Shinn BW, Farson DF, Denney PE (2005) Laser stabilisation of arc cathode spots in titanium welding. *Sci Technol Weld Joining* 10(4):475–481
 27. Sun Z, Lv Y, Xu B, Liu Y, Lin J, Wang K (2015) Investigation of droplet transfer behaviours in cold metal transfer (CMT) process on welding Ti-6Al-4V alloy. *Int J Adv Manuf Technol* 80(9–12):2007–2014
 28. Pardal G, Martina F, Williams S (2019) Laser stabilization of GMAW additive manufacturing of Ti-6Al-4V components. *J Mater Process Technol* 272:1–8
 29. Choudhury SS, Marya SK, Amirthalingam M (2021) Improving arc stability during wire arc additive manufacturing of thin-walled titanium components. *J Manuf Process* 66:53–69
 30. Lee TH, Kam DH, Oh JH, Kim C (2022) Ti-6Al-4V alloy deposition characteristics at electrode-negative polarity in the cold metal transfer-gas metal arc process. *J Market Res* 19:685–696
 31. Panchenko O, Kurushkin D, Isupov F, Naumov A, Kladov I, Surenkova M (2021) Gas metal arc welding modes in wire arc additive manufacturing of Ti-6Al-4V. *Materials (Basel)* 14(9):2457
 32. Gou J, Shen J, Hu S, Tian Y, Liang Y (2019) Microstructure and mechanical properties of as-built and heat-treated Ti-6Al-4V alloy prepared by cold metal transfer additive manufacturing. *J Manuf Process* 42:41–50
 33. Elitzer D, Höppel HW, Göken M, Baier D, Fuchs C, Bähr H et al (2020) Influence of wire arc additive manufacturing of Ti-6Al-4V on microstructure and mechanical properties for potential large-scale aviation parts. *MATEC Web Conf* 321:3037
 34. Lu Y (2018) The effects of inter-pass temperature on the microstructure and mechanical properties of Ti-6Al-4V alloy deposited by wire arc additive manufacturing (WAAM) [Master of Philosophy thesis]. University of Wollongong Thesis Collections, University of Wollongong
 35. Vázquez L, Rodríguez N, Rodríguez I, Alberdi E, Álvarez P (2020) Influence of interpass cooling conditions on microstructure and tensile properties of Ti-6Al-4V parts manufactured by WAAM. *Weld World* 64(8):1377–1388
 36. Birmingham MJ, Kent D, Zhan H, StJohn DH, Dargusch MS (2015) Controlling the microstructure and properties of wire arc additive manufactured Ti-6Al-4V with trace boron additions. *Acta Mater* 91:289–303
 37. Mereddy S, Birmingham MJ, StJohn DH, Dargusch MS (2017) Grain refinement of wire arc additively manufactured titanium by the addition of silicon. *J Alloy Compd* 695:2097–2103
 38. Mereddy S, Birmingham MJ, Kent D, Dehghan-Manshadi A, StJohn DH, Dargusch MS (2018) Trace carbon addition to refine microstructure and enhance properties of additive-manufactured Ti-6Al-4V. *JOM* 70(9):1670–1676
 39. Birmingham MJ, StJohn DH, Krynen J, Tedman-Jones S, Dargusch MS (2019) Promoting the columnar to equiaxed transition and grain refinement of titanium alloys during additive manufacturing. *Acta Mater* 168:261–274
 40. Yin B, Ma H, Wang J, Fang K, Zhao H, Liu Y (2017) Effect of CaF₂ addition on macro/microstructures and mechanical properties of wire and arc additive manufactured Ti-6Al-4V components. *Mater Lett* 190:64–66
 41. Martina F, Colegrove PA, Williams SW, Meyer J (2015) Microstructure of interpass rolled wire + arc additive manufacturing Ti-6Al-4V components. *Metall and Mat Trans A* 46(12):6103–6118
 42. Hönnige JR, Davis AE, Ho A, Kennedy JR, Neto L, Prangnell P et al (2020) The effectiveness of grain refinement by machine hammer peening in high deposition rate wire-arc AM Ti-6Al-4V. *Metall Mater Trans A* 51(7):3692–3703
 43. Davis AE, Kennedy JR, Ding J, Prangnell PB (2020) The effect of processing parameters on rapid-heating β recrystallization in inter-pass deformed Ti-6Al-4V wire-arc additive manufacturing. *Mater Charact* 163:110298
 44. Yang Y, Jin X, Liu C, Xiao M, Lu J, Fan H et al (2018) Residual Stress, Mechanical Properties, and Grain Morphology of Ti-6Al-4V Alloy Produced by Ultrasonic Impact Treatment Assisted Wire and Arc Additive Manufacturing. *Metals* 8(11):934
 45. McAndrew AR, Alvarez Rosales M, Colegrove PA, Hönnige JR, Ho A, Fayolle R et al (2018) Interpass rolling of Ti-6Al-4V wire + arc additively manufactured features for microstructural refinement. *Addit Manuf* 21:340–349
 46. Martina F, Williams SW, Colegrove P (2013) Improved microstructure and increased mechanical properties of additive manufacture produced Ti-6Al-4V by interpass cold rolling. 2013 International solid freeform fabrication symposium
 47. Martina F, Roy MJ, Szost BA, Terzi S, Colegrove PA, Williams SW et al (2016) Residual stress of as-deposited and rolled wire+arc additive manufacturing Ti-6Al-4V components. *Mater Sci Technol* 32(14):1439–1448
 48. Hönnige JR, Colegrove P, Williams S (2017) Improvement of microstructure and mechanical properties in Wire + Arc Additively Manufactured Ti-6Al-4V with Machine Hammer Peening. *Procedia Eng* 216:8–17
 49. Birmingham MJ, Nicastro L, Kent D, Chen Y, Dargusch MS (2018) Optimising the mechanical properties of Ti-6Al-4V components produced by wire + arc additive manufacturing with post-process heat treatments. *J Alloy Compd* 753:247–255
 50. Lütjering G, Williams JC (2007) *Titanium*, 2nd edn. Springer-Verlag, Berlin Heidelberg, Berlin Heidelberg New York
 51. Barge H-J, Schulze G (2018) *Werkstoffkunde*. Springer Vieweg Berlin, Heidelberg, Germany:309-355
 52. Caballero A, Ding J, Bandari Y, Williams S (2019) Oxidation of Ti-6Al-4V During Wire and Arc Additive Manufacture. *3D Print Addit Manuf* 6(2):91–8
 53. Wu B (2018) Quality improvement in wire arc additive manufacturing [Doctor of Philosophy thesis]. University of Wollongong Thesis Collections, University of Wollongong
 54. Ding J, Colegrove P, Martina F, Williams S, Wiktorowicz R, Palt MR (2015) Development of a laminar flow local shielding device for wire + arc additive manufacture. *J Mater Process Technol* 226:99–105
 55. Birmingham MJ, Thomson-Larkins J, St John DH, Dargusch MS (2018) Sensitivity of Ti-6Al-4V components to oxidation during out of chamber Wire + Arc Additive Manufacturing. *J Mater Process Technol* 258:29–37
 56. Ding D, Pan Z, Cuiuri D, Li H (2015) A multi-bead overlapping model for robotic wire and arc additive manufacturing (WAAM). *Robot Comput-Integr Manuf* 31:101–110
 57. Xiong J, Zhang G, Gao H, Wu L (2013) Modeling of bead section profile and overlapping beads with experimental validation for robotic GMAW-based rapid manufacturing. *Robot Comput-Integr Manuf* 29(2):417–423
 58. Eickhoff ST, Eagar TW (1990) Characterization of Spatter in Low-Current GMAW of Titanium Alloy Plate. *Weld J* 69(10):382
 59. Peters M, Leyens C (2002) *Titan und Titanlegierungen*. Wiley-VCH Verlag GmbH & Co. KGaA, Weinheim, Germany

60. Attanasio A, Gelfi M, Pola A, Ceretti E, Giardini C (2013) Influence of Material Microstructures in Micromilling of Ti6Al4V Alloy. *Materials (Basel)* 6(9):4268–4283
61. Bocchetta P, Chen L-Y, Tardelli JDC, Reis ACd, Almeraya-Calderón F, Leo P (2011) Passive Layers and Corrosion Resistance of Biomedical Ti-6Al-4V and β -Ti Alloys. *Coatings* 11(5):487
62. Vazquez L, Rodriguez MN, Rodriguez I, Alvarez P (2021) Influence of Post-Deposition Heat Treatments on the Microstructure and Tensile Properties of Ti-6Al-4V Parts Manufactured by CMT-WAAM. *Metals* 11(8):1161

Publisher's note Springer Nature remains neutral with regard to jurisdictional claims in published maps and institutional affiliations.